J|A|C|S
ARTICLES
Published on Web 07/10/2007

"Switching On" the Properties of Single-Molecule Magnetism in Triangular Manganese(III) Complexes

Theocharis C. Stamatatos,[†] Dolos Foguet-Albiol,[†] Sheng-Chiang Lee,[§] Constantinos C. Stoumpos,[‡] Catherine P. Raptopoulou,[∥] Aris Terzis,[∥] Wolfgang Wernsdorfer,[⊥] Stephen O. Hill,[§] Spyros P. Perlepes,*[,‡] and George Christou*[,†]

Contribution from the Department of Chemistry, University of Florida, Gainesville, Florida 32611, Department of Chemistry, University of Patras, Patras 26504, Greece, Department of Physics, University of Florida, Gainesville, Florida 32611, Institute of Materials Science, NCSR "Demokritos", 15310 Aghia Paraskevi Attikis, Greece, and Institut Néel, CNRS/UJF, BP 166, 25 Avenue des Martyrs, 38042 Grenoble, Cedex 9, France

Received April 5, 2007; E-mail: christou@chem.ufl.edu; perlepes@patreas.upatras.gr

Abstract: The reaction between oxide-centered, triangular $[Mn^{III}_3O(O_2CR)_6(py)_3](ClO_4)$ (R = Me (**1**), Et (**2**), Ph (**3**)) compounds and methyl 2-pyridyl ketone oxime (mpkoH) affords a new family of Mn/carboxylato/oximato complexes, $[Mn^{III}_3O(O_2CR)_3(mpko)_3](ClO_4)$ [R = Me (**4**), Et (**5**), and Ph (**6**)]. As in **1**−**3**, the cations of **4**−**6** contain an $[Mn^{III}_3(\mu_3\text{-}O)]^{7+}$ triangular core, but with each Mn_2 edge now bridged by an $\eta^1{:}\eta^1{:}\mu$-RCO_2^- and an $\eta^1{:}\eta^1{:}\eta^1{:}\mu$-mpko$^-$ group. The tridentate binding mode of the latter causes a buckling of the formerly planar $[Mn^{III}_3(\mu_3\text{-}O)]^{7+}$ core, resulting in a relative twisting of the three Mn^{III} octahedra and the central O^{2-} ion now lying ∼0.3 Å above the Mn_3 plane. This structural distortion leads to ferromagnetic exchange interactions within the molecule and a resulting $S = 6$ ground state. Fits of dc magnetization data for **4**−**6** collected in the 1.8−10.0 K and 10−70 kG ranges confirmed $S = 6$ ground states, and gave the following D and g values: -0.34 cm^{-1} and 1.92 for **4**, -0.34 cm^{-1} and 1.93 for **5**, and -0.35 cm^{-1} and 1.99 for **6**, where D is the axial zero-field splitting (anisotropy) parameter. Complexes **4**−**6** all exhibit frequency-dependent out-of-phase (χ''_M) ac susceptibility signals suggesting them possibly to be single-molecule magnets (SMMs). Relaxation rate vs T data for complex **4** down to 1.8 K obtained from the χ''_M vs T studies were supplemented with rate vs T data measured to 0.04 K via magnetization vs time decay studies, and these were used to construct Arrhenius plots from which was obtained the effective barrier to relaxation (U_{eff}) of 10.9 K. Magnetization vs dc field sweeps on single-crystals of **4**·$3CH_2Cl_2$ displayed hysteresis loops exhibiting steps due to quantum tunneling of magnetization (QTM). The loops were essentially temperature-independent below ∼0.3 K, indicating only ground-state QTM between the lowest-lying $M_s = \pm 6$ levels. Complexes **4**−**6** are thus confirmed as the first triangular SMMs. High-frequency EPR spectra of single crystals of **4**·$3CH_2Cl_2$ have provided precise spin Hamiltonian parameters, giving $D = -0.3$ cm^{-1}, $B_4^0 = -3 \times 10^{-5}$ cm^{-1}, and $g = 2.00$. The spectra also suggest a significant transverse anisotropy of $E \geq 0.015$ cm^{-1}. The combined work demonstrates the feasibility that structural distortions of a magnetic core imposed by peripheral ligands can "switch on" the properties of an SMM.

Introduction

Single-molecule magnets (SMMs) are individual molecules that function as nanoscale magnetic particles.[1−3] Although molecular, these species display superparamagnetic properties normally associated with much larger nanoscale magnetic particles, and thus below their blocking temperature (T_B) they function as magnets.[4−5] As a result, they represent potential molecular memory elements for specialized, molecule-based information storage devices, as well as potential quantum bits for quantum information processing.[6] SMMs derive their

[†] Department of Chemistry, University of Florida.
[‡] Department of Chemistry, University of Patras.
[§] Department of Physics, University of Florida.
[∥] NCSR "Demokritos".
[⊥] Institut Néel, CNRS/UJF.

(1) (a) Sessoli, R.; Tsai, H.-L.; Schake, A. R.; Wang, S.; Vincent, J. B.; Folting, K.; Gatteschi, D.; Christou, G.; Hendrickson, D. N. *J. Am. Chem. Soc.* **1993**, *115*, 1804. (b) Sessoli, R.; Gatteschi, D.; Caneschi, A.; Novak, M. A. *Nature* **1993**, *365*, 141.
(2) Christou, G.; Gatteschi, D.; Hendrickson, D. N.; Sessoli, R. *MRS Bull.* **2000**, *25*, 66.
(3) (a) Christou, G. *Polyhedron* **2005**, *24*, 2065. (b) Aromi, G.; Brechin, E. K. *Struct. Bonding (Berlin)* **2006**, *122*, 1.
(4) (a) Bircher, R.; Chaboussant, G.; Dobe, D.; Güdel, H. U.; Oshsenbein, S. T.; Sieber, A.; Waldmann, O *Adv. Funct. Mater.* **2006**, *16*, 209. (b) Gatteschi, D.; Sessoli, R. *Angew. Chem., Int. Ed.* **2003**, *42*, 268.
(5) (a) Aubin, S. M. J.; Gilley, N. R.; Pardi, L.; Krzystek, J.; Wemple, M. W.; Brunel, L.- C.; Maple, M. B.; Christou, G.; Hendrickson, D. N. *J. Am. Chem. Soc.* **1998**, *120*, 4991. (b) Oshio, H.; Nakano, M. *Chem. Eur. J.* **2005**, *11*, 5178.
(6) (a) Tejada, J.; Chudnovsky, E. M.; del Barco, E.; Hernandez, J. M.; Spiller, T. P. *Nanotechnology* **2001**, *12*, 181. (b) Wernsdorfer, W.; Aliaga-Acalde, N.; Hendrickson, D. N.; Christou, G. *Nature* **2002**, *416*, 406. (c) Hill, S.; Edwards, R. S.; Aliaga-Acalde, N.; Christou, G. *Science* **2003**, *302*, 1015.

 10.1021/ja072194p CCC: $37.00

properties from the combination of a large ground-state spin quantum number (S) and a magnetoanisotropy of the easy-axis (Ising)-type (negative zero-field splitting parameter, D), rather than from intermolecular interactions and long-range ordering as in traditional magnets. This combination leads to a significant barrier (U) to relaxation (reorientation) of the magnetization vector, whose maximum value is given by $S^2|D|$ or $(S^2 - 1/4)|D|$ for integer and half-integer spin, respectively. Experimentally, a SMM shows superparamagnet-like properties, exhibiting both frequency-dependent out-of-phase ac magnetic susceptibility signals, and hysteresis in a plot of magnetization vs applied DC magnetic field. Thus, SMMs represent a molecular (or bottom-up) approach to nanoscale magnetism, and they are consequently also referred to occasionally as molecular nanomagnets. In addition, they clearly straddle the classical/quantum interface, displaying not only the classical property of magnetization hysteresis but also the quantum properties of tunneling of the magnetization (QTM)[7] through the anisotropy barrier, and quantum phase interference.[8]

To date, the most studied SMMs are the mixed-valent $[Mn_{12}O_{12}(O_2CR)_{16}(H_2O)_4]$ ($Mn^{III}_8Mn^{IV}_4$; R = various) family with an $S = 10$ ground state.[1,9] There are now also many other structural types displaying SMM behavior, the vast majority of them being Mn complexes. This is because Mn clusters often display relatively large ground state S values, as well as relatively large (and negative) D values associated with the presence of Jahn−Teller distorted Mn^{III} atoms. However, the concomitant presence of Mn^{II} atoms, which give weak exchange interactions with Mn^{III}, often lead to SMMs with low-lying excited states and relatively increased relaxation rates.[10] Thus, the SMMs with the largest relaxation barriers are currently either Mn^{III}_x or mixed-valent Mn^{III}/Mn^{IV} species. The former currently comprise Mn_2,[11] Mn_4,[12] Mn_6,[13] Mn_{26},[14] and Mn_{84}[15] complexes, including the Mn_6 complex with the highest barrier yet discovered.[16]

As part of the search for new SMMs, there are two general strategies: one is to seek completely new structural types that might provide the desired properties, and the second is to modify known structural types that may or may not already be SMMs in their own right. Most groups currently seeking new SMMs are employing the former approach, but the present work concerns the latter. Indeed, the first significant modification of an SMM was the one- and two-electron reduction of the $[Mn_{12}O_{12}(O_2CR)_{16}(H_2O)_4]$ family, the products still being SMMs with $S = {}^{19}/_2$[17] and 10[17,18] ground states, respectively. More recently, we demonstrated "spin tweaking", the conversion of an already high-spin Mn_{25} SMM with $S = {}^{51}/_2$ into a structurally similar one with $S = {}^{61}/_2$ by modification of the peripheral ligands.[19] A third approach involved the conversion of a low-spin cluster to a high-spin SMM by replacement of bridging OH^- groups (that give antiferromagnetic coupling) in Fe^{II} clusters with end-on N_3^- bridges (that give ferromagnetic coupling), although the core structure did change significantly as a result.[20] In the present work, we report a distinctly different approach within this strategy of modifying known complexes, the conversion of certain low-spin complexes into high-spin ones without changing the core. The former are members of the family of triangular $[M_3O(O_2CR)_6L_3]^{n+}$ ($n = 0, 1$) complexes containing the $[M_3(\mu_3\text{-O})]$ core and known for many transition metals.[21] These are antiferromagnetically coupled with small S values, and they are therefore not SMMs.[14,21] However, we shall show that certain M = Mn members of this family can be converted to products with the same $[Mn_3(\mu_3\text{-O})]$ core but which are now ferromagnetically coupled. This has been accomplished from reactions with 2-pyridyl ketone oximes (Scheme 1), part of a longstanding interest by many groups in the structures and properties of transition-metal oxime compounds.[22−28] We shall

(7) (a) Friedman, J. R.; Sarachik, M. P. *Phys. Rev. Lett.* **1996**, *76*, 3830. (b) Thomas, L.; Lionti, L.; Ballou, R.; Gatteschi, D.; Sessoli, R.; Barbara, B. *Nature* **1996**, *383*, 145.

(8) (a) Wernsdorfer, W.; Sessoli, R. *Science* **2000**, 2417. (b) Wernsdorfer, W.; Soler, M.; Christou, G.; Hendrickson, D. N. *J. Appl. Phys.* **2002**, *91*, 7164. (c) Wernsdorfer, W.; Chakov, N. E.; Christou, G. *Phys. Rev. Lett.* **2005**, *95*, 037203 (1−4).

(9) (a) Lis. T. *Acta Crystallogr.* **1980**, *B36*, 2042. (b) Artus, P.; Boskovic, C.; Yoo, Y.; Streib, W. E.; Brunel, L.-C.; Hendrickson, D. N.; Christou, G. *Inorg. Chem.* **2001**, *40*, 4199. (c) Ruiz, D.; Sun, Z.; Albela, B.; Folting, K.; Ribas, J.; Christou, G.; Hendrickson, D. N. *Angew. Chem., Int. Ed.* **1998**, *37*, 300. (d) Aubin, S. M. J.; Sun, Z.; Guzei, I. A.; Rheingold, A. L.; Christou, G.; Hendrickson, D. N. *J. Chem. Soc., Chem. Commun.* **1997**, 2239. (e) Boskovic, C.; Pink, M.; Huffman, J. C.; Hendrickson, D. N.; Christou, G. *J. Am. Chem. Soc.* **2001**, *123*, 9914. (f) Soler, M.; Artus, P.; Folting, K.; Huffman, J. C.; Hendrickson, D. N.; Christou, G. *Inorg. Chem.* **2001**, *40*, 4902. (g) Chakov, N. E.; Abboud, K. A.; Zakharov, L. N.; Rheingold, A. L.; Hendrickson, D. N.; Christou, G. *Polyhedron* **2003**, *22*, 1759. (h) Chakov, N. E.; Lawrence, J.; Harter, A. G.; Hill, S. O.; Dalal, N. S.; Wernsdorfer, W.; Abboud, K. A.; Christou, G. *J. Am. Chem. Soc.* **2006**, *128*, 6975.

(10) (a) Aliaga-Alcade, N.; Edwards, R. S.; Hill, S. O.; Wernsdorfer, W.; Folting, K.; Christou, G. *J. Am. Chem. Soc.* **2004**, *126*, 12503. (b) Yoo, J.; Brechin, E. K.; Yamaguchi, A.; Nakano, M.; Huffman, J. C.; Maniero, A. L.; Brunel, L.- C.; Awaga, K.; Ishimoto, H.; Christou, G.; Hendrickson, D. N. *Inorg. Chem.* **2000**, *39*, 3615. (c) Brechin, E. K.; Yoo, J.; Nakano, M.; Huffman, J. C.; Hendrickson, D. N.; Christou, G. *Chem. Commun.* **1999**, 783. (d) Wang, S.; Wemple, M. S.; Tsai, H.-L.; Folting, K.; Huffman, J. C.; Hagen, K. S.; Hendrickson, D. N.; Christou, G. *Inorg. Chem.* **2000**, *39*, 1501. (e) Wemple, M. W.; Tsai, H.-L.; Folting, K.; Hendrickson, D. N.; Christou, G. *Inorg. Chem.* **1993**, *32*, 2025. (f) Aliaga, N.; Folting, K.; Hendrickson, D. N.; Christou, G. *Polyhedron* **2001**, *20*, 1273.

(11) (a) Rajaraman, G.; Sanudo, E. C.; Helliwell, M.; Piligkos, S.; Wernsdorfer, W.; Christou, G.; Brechin, E. K. *Polyhedron* **2005**, *24*, 2450. (b) Miyasaka, H.; Clérac, R.; Wernsdorfer, W.; Lecren, L.; Bonhomme, C.; Sugiura, K.; Yamashita, M. *Angew. Chem., Int. Ed.* **2004**, *43*, 2801.

(12) Milios, C. J.; Prescimone, A.; Mishra, A.; Parsons, S.; Wernsdorfer, W.; Christou, G.; Perlepes, S. P.; Brechin, E. K. *Chem. Commun.* **2007**, 153.

(13) (a) Milios, C. J.; Raptopoulou, C. P.; Terzis, A.; Lloret, F.; Vicente, R.; Perlepes, S. P.; Escuer, A. *Angew. Chem., Int. Ed.* **2004**, *43*, 210. (b) Milios, C. J.; Vinslava, A.; Wood, P. A.; Parsons, S.; Wernsdorfer, W.; Christou, G.; Perlepes, S. P.; Brechin, E. K. *J. Am. Chem. Soc.* **2007**, *129*, 8.

(14) Jones, L. F.; Rajaraman, G.; Brockman, J.; Murugescu, M.; Sanudo, E. C.; Raftery, J.; Teat, S. J.; Wernsdorfer, W.; Christou, G.; Brechin, E. K.; Collison, D. *Chem. Eur. J.* **2004**, *10*, 5180.

(15) (a) Tasiopoulos, A. J.; Vinslava, A.; Wernsdorfer, W.; Abboud, K. A.; Christou, G. *Angew. Chem., Int. Ed.* **2004**, *43*, 2117. (b) Christou, G. *Polyhedron* **2005**, *24*, 2065.

(16) Milios, C. J.; Vinslava, A.; Wernsdorfer, W.; Moggach, S.; Parsons, S.; Perlepes, S. P.; Christou, G.; Brechin, E. K. *J. Am. Chem. Soc.* **2007**, *129*, 2754.

(17) (a) Eppley, H.- J.; Tsai, H.- L.; Vries, N. de; Folting, K.; Christou, G.; Hendrickson, D. N. *J. Am. Chem. Soc.* **1995**, *117*, 301. (b) Chakov, N. E.; Soler, M.; Wernsdorfer, W.; Abboud, K. A.; Christou, G. *Inorg. Chem.* **2005**, *44*, 5304. (c) Aubin, S. M. J.; Sun, Z.; Pardi, L.; Krzystek, J.; Folting, K.; Brunel, L.-C.; Rheingold, A. L.; Christou, G.; Hendrickson, D. N. *Inorg. Chem.* **1999**, *38*, 5329.

(18) (a) Soler, M.; Wernsdorfer, W.; Abboud, K. A.; Huffman, J. C.; Davidson, E. R.; Hendrickson, D. N.; Christou, G. *J. Am. Chem. Soc.* **2003**, *125*, 3576. (b) Soler, M.; Wernsdorfer, W.; Abboud, K. A.; Hendrickson, D. N.; Christou, G. *Polyhedron* **2003**, *22*, 1777. (c) Soler, M.; Chandra, S. K.; Ruiz, D.; Davidson, E. R.; Hendrickson, D. N.; Christou, G. *Chem. Commun.* **2000**, 2417. (d) Soler, M.; Chandra, S. K.; Ruiz, D.; Huffman, J. C.; Hendrickson, D. N.; Christou, G. *Polyhedron* **2001**, *20*, 1279−1283.

(19) Stamatatos, Th. C.; Abboud, K. A.; Wernsdorfer, W.; Christou, G. *Angew. Chem., Int. Ed.* **2007**, *46*, 884.

(20) Boudalis, A. K.; Donnadieu, B.; Nastopoulos, V.; Clemente-Juan, J. M.; Mari, A.; Sanakis, Y.; Tuchagues, J.-P.; Perlepes, S. P. *Angew. Chem., Int. Ed.* **2004**, *43*, 2266.

(21) (a) Vincent, J. B.; Chang, H.- R.; Folting, K.; Huffman, J. C.; Christou, G.; Hendrickson, D. N. *J. Am. Chem. Soc.* **1987**, *109*, 5703 and references therein. (b) McCusker, J. K.; Jang, H. G.; Wang, S.; Christou, G.; Hendrickson, D. N. *Inorg. Chem.* **1992**, *31*, 1874−1880. (c) Vincent, J. B.; Tsai, H.-L.; Blackman, A. G.; Wang, S.; Boyd, P. D. W.; Folting, K.; Huffman, J. C.; Lobkovsky, E. B.; Hendrickson, D. N.; Christou, G. *J. Am. Chem. Soc.* **1993**, *115*, 12353.

(22) Chaudhuri, P. *Coord. Chem. Rev.* **2003**, *243*, 143.

Scheme 1

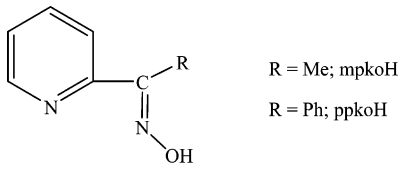

also show that the resulting products possess a significant *D* value, and that this together with a high *S* value of $S = 6$ has led to the products being the first examples of SMMs with a triangular structure. Portions of this work have been previously communicated.[29]

Experimental Section

Syntheses. All manipulations were performed under aerobic conditions using chemicals and solvents as received unless otherwise stated. $Mn(O_2CEt)_2 \cdot 4H_2O$,[30] $Mn(O_2CPh)_2 \cdot 2H_2O$,[31] $NBu^n_4MnO_4$,[21] $[Mn_3O(O_2CR)_6(py)_3]$ (R = Me, Et; py = pyridine),[21] $[Mn_3O(O_2CPh)_6(py)_2(H_2O)]$,[21] and $[Mn_3O(O_2CR)_6(py)_3](ClO_4)$ (R = Me (**1**), Et (**2**), Ph (**3**))[21] were prepared as described elsewhere. mpkoH was synthesized as previously reported.[32] *WARNING: Appropriate care should be taken in the use of $NBu^n_4MnO_4$, and readers are referred to the detailed warning given elsewhere.[21] Perchlorate salts are potentially explosive; such compounds should be synthesized and used in small quantities, and treated with utmost care at all times.*

$[Mn_3O(O_2CMe)_3(mpko)_3](ClO_4)$ (4). Method A. To a stirred, brown solution of complex **1** (0.18 g, 0.20 mmol) in MeOH/MeCN (15 mL, 1:2 v/v) was added solid mpkoH (0.08 g, 0.60 mmol). The resulting dark-brown solution was stirred for 15 min, after which time all the mpkoH had dissolved. The solution was evaporated to dryness under reduced pressure and the residue redissolved in CH_2Cl_2 (25 mL) to give an almost black solution. The solution was filtered and layered with hexanes (50 mL). After 2 days, dark-red prismatic crystals of **4**·$3CH_2Cl_2$ were collected by filtration, washed with CH_2Cl_2 (2 × 5 mL) and Et_2O (2 × 5 mL), and dried in air; the yield was ∼90%. Anal. Calcd for **4**: C, 37.59; H, 3.50; N, 9.74. Found: C, 37.32; H, 3.49; N, 9.54. Selected IR data (cm^{-1}): 3418 (mb), 1602 (vs), 1568 (vs), 1475 (m), 1390 (s), 1338 (s), 1263 (m), 1180 (s), 1108 (s), 1086 (vs), 1048 (m), 940 (w), 778 (m), 690 (s), 660 (s), 624 (m), 564 (w), 493 (w), 449 (w), 417 (m).

Method B. To a stirred, brown solution of $[Mn_3O(O_2CMe)_6(py)_3]$ (0.08 g, 0.10 mmol) in EtOH/MeCN (15 mL; 1:2 v/v) was added solid mpkoH (0.04 g, 0.30 mmol). The resulting dark-brown solution was stirred for 20 min, during which time $NaClO_4 \cdot H_2O$ (0.03 g, 0.20 mmol) was added in small amounts without any noticeable color change. The solution was evaporated to dryness under reduced pressure and the oily residue redissolved in CH_2Cl_2 (20 mL) to give an almost black solution. The solution was filtered and layered with Et_2O (40 mL). After 5 days, dark-red prismatic crystals were collected by filtration, washed with CH_2Cl_2 (2 × 5 mL) and Et_2O (2 × 5 mL), and dried in air; the yield was ∼50%. The identity of the product was confirmed by elemental analysis (C, H, N) and IR spectroscopic comparison with material from Method A.

Method C. To a stirred, dark-brown solution of $Mn(O_2CMe)_2 \cdot 4H_2O$ (0.07 g, 0.30 mmol) and $NBu^n_4MnO_4$ (0.04 g, 0.10 mmol) in EtOH/MeCN (15 mL; 1:2 v/v) was added solid mpkoH (0.04 g, 0.30 mmol). The resulting dark-brown solution was stirred for 30 min, during which time $NBu^n_4ClO_4$ (0.10 g, 0.30 mmol) was added in small amounts without any noticeable color change. The solution was evaporated to dryness under reduced pressure and the microcrystalline residue redissolved in CH_2Cl_2 (20 mL) to give an essentially black solution. The solution was filtered and layered with hexanes (40 mL). After 5 days, dark-red prismatic crystals were collected by filtration, washed with CH_2Cl_2 (2 × 5 mL) and hexanes (2 × 5 mL), and dried in air; the yield was ∼45%. The identity of the product was confirmed by elemental analysis (C, H, N) and IR spectroscopic comparison with material from Method A.

$[Mn_3O(O_2CEt)_3(mpko)_3](ClO_4)$ (5). Method A. To a stirred, brown solution of complex **2** (0.19 g, 0.20 mmol) in MeOH/MeCN (15 mL, 1:2 v/v) was added solid mpkoH (0.08 g, 0.60 mmol). The resulting dark-brown mixture was stirred for 15 min, during which time all the mpkoH dissolved. The solution was evaporated to dryness under reduced pressure and the residue redissolved in CH_2Cl_2 (25 mL) to give an essentially black solution. The solution was filtered and layered with Et_2O (50 mL). After 3 days, dark-red prismatic crystals of **5**·$1.2CH_2Cl_2 \cdot 1.4H_2O$ were collected by filtration, washed with CH_2Cl_2 (2 × 5 mL) and Et_2O (2 × 5 mL), and dried in vacuo over silica gel; the yield was ∼ 85%. The dried material is hygroscopic and was analyzed as **5**·H_2O. Anal. Calcd for **5**·H_2O: C, 39.04; H, 4.15; N, 9.11. Found: C, 39.24; H, 3.82; N, 9.07. Selected IR data (cm^{-1}): 3452 (mb), 2974 (m), 2938 (w), 1602 (vs), 1578 (vs), 1474 (m), 1465 (m), 1392 (s), 1362 (m), 1282 (m), 1184 (s), 1108 (s), 1088 (vs), 1048 (m), 884 (w), 814 (w), 776 (m), 700 (m), 662 (m), 624 (m), 564 (w), 492 (w), 452 (w).

Method B. To a stirred, brown solution of $[Mn_3O(O_2CEt)_6(py)_3]$ (0.09 g, 0.10 mmol) in a solvent mixture comprising EtOH/MeCN (15 mL, 1:2 v/v) was added solid mpkoH (0.04 g, 0.30 mmol). The resulting dark-brown solution was stirred for 50 min, during which time $NaClO_4 \cdot H_2O$ (0.03 g, 0.20 mmol) was added in small amounts without any noticeable color change. The solution was evaporated to dryness under reduced pressure and the oily residue redissolved in CH_2Cl_2 (15 mL) to give a black solution. The solution was filtered and layered with Et_2O (30 mL). After 4 days, dark-red prismatic crystals were collected by filtration, washed with CH_2Cl_2 (2 × 5 mL) and Et_2O (2 × 5 mL), and dried in air; the yield was ∼55%. The identity of the product was confirmed by elemental analysis (C, H, N) and IR spectroscopic comparison with material from Method A.

Method C. To a stirred, dark-brown solution of $Mn(O_2CEt)_2 \cdot 4H_2O$ (0.08 g, 0.30 mmol) and $NBu^n_4MnO_4$ (0.04 g, 0.10 mmol) in MeOH/MeCN (15 mL, 1:2 v/v) was added solid mpkoH (0.04 g, 0.30 mmol). The resulting dark-brown solution was stirred for 30 min, during which time $NBu^n_4ClO_4$ (0.10 g, 0.30 mmol) was added in small amounts without any noticeable color change. The solution was evaporated to dryness under reduced pressure and the microcrystalline residue redissolved in CH_2Cl_2 (20 mL) to give a black solution. This was filtered and layered with hexanes (40 mL). After 7 days, dark-red prismatic crystals were collected by filtration, washed with CH_2Cl_2 (2 × 5 mL) and Et_2O (2 × 5 mL), and dried in air; the yield was ∼40%. The identity of the product was confirmed by elemental analysis (C, H, N) and IR spectroscopic comparison with material from Method A.

$[Mn_3O(O_2CPh)_3(mpko)_3](ClO_4)$ (6). Method A. To a stirred, brown solution of complex **3** (0.25 g, 0.20 mmol) in MeOH/MeCN (15 mL,

(23) (a) Chaudhuri, P.; Hess, M.; Weyhermüller, T.; Bill, E.; Haupt, H.- J.; Flörke, U. *Inorg. Chem. Commun.* **1998**, *1*, 39. (b) Burdinski, D.; Birkelbach, F.; Weyhermüller, T.; Flörke, U.; Haupt, H.- J.; Lengen, M.; Trautwein, A. X.; Bill, E.; Wieghardt, K.; Chaudhuri, P. *Inorg. Chem.* **1998**, *37*, 1009.
(24) Thorpe, J. M.; Beddoes, R. L.; Collison, D.; Garner, C. D.; Helliwell, M.; Holmes, J. M.; Tasker, P. A. *Angew. Chem., Int. Ed.* **1999**, *38*, 1119.
(25) Chaudhuri, P.; Winter, M.; Birkelbach, F.; Fleischhauer, P.; Haase, W.; Flörke, U.; Haupt, H.- J. *Inorg. Chem.* **1991**, *30*, 4291.
(26) Miyasaka, H.; Clérac, R. *Bull. Chem. Soc. Jpn.* **2005**, *78*, 1725 and references therein.
(27) Mori, F.; Nyui, T.; Ishida, T.; Nogami, T.; Choi, K.- Y.; Nojiri, H. *J. Am. Chem. Soc.* **2006**, *128*, 1440.
(28) For a comprehensive review, see: Milios, C. J.; Stamatatos, Th. C.; Perlepes, S. P. *Polyhedron* **2006**, *25*, 134 and references therein.
(29) Stamatatos, Th. C.; Foguet-Albiol, D.; Stoumpos, C. C.; Raptopoulou, C. P.; Terzis, A.; Wernsdorfer, W.; Perlepes, S. P.; Christou, G. *J. Am. Chem. Soc.* **2005**, *127*, 15380.
(30) Aromi, G.; Bhaduri, S.; Artús, P.; Huffman, J. C.; Hendrickson, D. N.; Christou, G. *Polyhedron* **2002**, *21*, 1779.
(31) Wemple, M. W.; Tsai, H. -L.; Wang, S.; Claude, J. P.; Streib, W. E.; Huffman, J. C.; Hendrickson, D. N.; Christou, G. *Inorg. Chem.* **1996**, *35*, 6437.
(32) Orama, M.; Saarinen, H.; Korvenranta, J. *J. Coord. Chem.* **1990**, *22*, 183.

Table 1. Crystallographic Data for Complexes **4**·$3CH_2Cl_2$, **5**·$1.2CH_2Cl_2$·$1.4H_2O$, and **6**·$4CH_2Cl_2$

parameter	**4**·$3CH_2Cl_2$	**5**·$1.2CH_2Cl_2$·$1.4H_2O$	**6**·$4CH_2Cl_2$
formula	$C_{33}H_{36}N_6O_{14}Cl_7Mn_3$	$C_{31.2}H_{41.2}N_6O_{15.4}Cl_{3.4}Mn_3$	$C_{46}H_{44}N_6O_{14}Cl_9Mn_3$
fw, g mol^{-1}	1117.54	1032.06	1388.76
crystal system	monoclinic	monoclinic	monoclinic
space group	$P2_1/c$	$P2_1/c$	$P2_1/n$
α, Å	12.986(5)	12.988(5)	19.700(9)
b, Å	14.978(6)	15.111(6)	10.746(5)
c, Å	23.150(10)	27.740(10)	28.614(14)
β, deg	93.82(2)	94.820(10)	107.53(2)
V, Å^3	4493(3)	5425(4)	5776(5)
Z	4	4	4
T, °C	25	25	25
radiation, Å[a]	0.71073 (Mo Ka)	0.71073 (Mo Ka)	1.54180 (Cu Ka)
ρ_{calc}, g cm^{-3}	1.276	1.108	1.206
μ, mm^{-1}	0.947	0.787	6.172
R1[b]	0.0556[c]	0.0621[d]	0.0563[e]
wR2[b]	0.1515[c]	0.1691[d]	0.1470[e]

[a] Graphite monochromator. [b] $w = 1/[\sigma^2(F_o^2) + (aP)^2 + bP]$ and $P = \max(F_o^2,0) + 2F_c^2/3$; $R1 = \Sigma(|F_o| - |F_c|)/\Sigma(|F_o|)$ and $wR2 = \{\Sigma[w(F_o^2 - F_c^2)^2]/\Sigma[w(F_o^2)^2]\}^{1/2}$. [c] For 4111 reflections with $I > 2\sigma(I)$. [d] For 4874 reflections with $I > 2\sigma(I)$. [e] For 5504 reflections with $I > 2\sigma(I)$.

1:2 v/v) was added solid mpkoH (0.08 g, 0.60 mmol). The resulting dark-brown mixture was stirred for 25 min, during which time all the mpkoH dissolved. The solution was evaporated to dryness under reduced pressure and the residue redissolved in CH_2Cl_2 (25 mL) to give an essentially black solution. The solution was filtered and layered with Et_2O (50 mL). After 4 days, dark-red prismatic crystals were collected by filtration, washed with CH_2Cl_2 (2 × 5 mL) and Et_2O (2 × 5 mL), and dried in vacuo over silica gel; the yield was ∼ 80%. The dried material is hygroscopic and was analyzed as **6**·$2.5H_2O$. Anal. Calcd for **6**·$2.5H_2O$: C, 46.11; H, 3.78; N, 7.68. Found: C, 46.37; H, 3.35; N, 7.19. Selected IR data (cm^{-1}): 3444 (mb), 2928 (w), 1602 (s), 1560 (vs), 1476 (m), 1448 (w), 1366 (vs), 1264 (w), 1182 (m), 1110 (s), 1086 (s), 1046 (m), 836 (w), 776 (m), 720 (m), 665 (m), 624 (m), 474 (m).

Method B. To a stirred, brown solution of $[Mn_3O(O_2CPh)_6(py)_2(H_2O)]$ (0.12 g, 0.10 mmol) in EtOH/MeCN (15 mL, 1:2 v/v) was added solid mpkoH (0.04 g, 0.30 mmol). The resulting dark-brown solution was stirred for 30 min, during which time $NaClO_4$·H_2O (0.03 g, 0.20 mmol) was added in small amounts without any noticeable color change. The solution was evaporated to dryness under reduced pressure and the oily residue redissolved in CH_2Cl_2 (15 mL) to give an essentially black solution. This was filtered and layered with Et_2O (30 mL). After 6 days, dark-red prismatic crystals were collected by filtration, washed with CH_2Cl_2 (2 × 5 mL) and Et_2O (2 × 5 mL), and dried in air; the yield was ∼ 45%. The IR spectrum was identical to that of material from Method A.

Method C. To a stirred, dark-brown solution of $Mn(O_2CPh)_2$·$2H_2O$ (0.10 g, 0.30 mmol) and $NBu^n_4MnO_4$ (0.04 g, 0.10 mmol) in MeOH/MeCN (15 mL, 1:2 v/v) was added solid mpkoH (0.04 g, 0.30 mmol). The resulting dark-brown solution was stirred for 30 min, during which time $NBu^n_4ClO_4$ (0.10 g, 0.30 mmol) was added in small amounts without any noticeable color change. The solution was evaporated to dryness under reduced pressure and the microcrystalline product redissolved in CH_2Cl_2 (20 mL) to give a black solution. The solution was filtered and layered with hexanes (40 mL). After 7 days, dark-red prismatic crystals were collected by filtration, washed with CH_2Cl_2 (2 × 5 mL) and hexanes (2 × 5 mL), and dried in air; the yield was ∼ 40%. The identity of the product was confirmed by elemental analyses (C, H, N) and IR spectroscopic comparison with material from Method A.

X-ray Crystallography. Dark-red prismatic crystals of **4**·$3CH_2Cl_2$ (0.75 × 0.45 × 0.10 mm), **5**·$1.2CH_2Cl_2$·$1.4H_2O$ (0.75 × 0.40 × 0.25 mm), and **6**·$4CH_2Cl_2$ (0.50 × 0.20 × 0.15 mm) were mounted in capillaries. Diffraction measurements for **4**·$3CH_2Cl_2$ and **5**·$1.2CH_2Cl_2$·$1.4H_2O$ were made on a Crystal Logic Dual Goniometer diffractometer using graphite monochromated Mo Kα radiation, whereas diffraction measurements for **6**·$4CH_2Cl_2$ were made on a $P2_1$ Nicolet diffractometer upgraded by Crystal Logic using graphite monochromated Cu Kα radiation. Crystal data and parameters for data collection and refinement are listed in Table 1.

For **4**·$3CH_2Cl_2$, unit cell dimensions were determined and refined by using the angular settings of 25 automatically centered reflections in the range $11 < 2\theta < 23°$. Intensity data were recorded using a $\theta-2\theta$ scan to $2\theta_{max} = 45°$, with scan speed 1.5° min^{-1} and scan range $1.6 + \alpha_1\alpha_2$ separation. The crystals showed poor diffraction ability (despite their sufficient size), and the data were collected in increasing 2θ shells. In the last data shell collection (45−50°) the observed data were less than 50% of the collected ones. Thus, the data above 45° have been omitted during the refinement of the structure by using the corresponding OMIT card of the SHELXL program. Three standard reflections that were monitored every 97 reflections showed less than 3% variation and no decay. Lorentz, polarization, and Ψ-scan absorption corrections were applied using Crystal Logic software. Symmetry equivalent data were averaged with $R_{int} = 0.0264$ to give 5282 independent reflections from a total of 5426 collected. The structure was solved by direct methods using SHELXS-86[33] and refined by full-matrix least-squares techniques on F^2 with SHELXL-97[34] using 5282 reflections and refining 466 parameters. The compound crystallizes with three crystallographically independent CH_2Cl_2 solvate molecules per trinuclear complex. The solvate molecules showed large thermal motion parameters on their full occupancy; thus, the SQUEEZE option of PLATON program was used to calculate and remove their contribution from the overall intensity data. All hydrogen atoms were introduced at calculated positions as riding on bonded atoms. All non-hydrogen atoms were refined anisotropically. The maximum and minimum residual peaks in the final difference map were 0.485 and −0.283 e Å^{-3}, respectively.

For **5**·$1.2CH_2Cl_2$·$1.4H_2O$, unit cell dimensions were determined and refined by using the angular settings of 25 automatically centered reflections in the range $11 < 2\theta < 23°$. Intensity data were recorded using a $\theta-2\theta$ scan to $2\theta_{max} = 47.5°$, with scan speed 1.5 ° min^{-1} and scan range $1.6 + \alpha_1\alpha_2$ separation. The crystals showed poor diffraction ability (despite their sufficient size), and the data were collected in increasing 2θ shells. In the last data shell collection (45−47.5°) the observed data were less than 50% of the collected ones. Thus, the data collection was terminated. Three standard reflections that were monitored every 97 reflections showed less than 3% variation and no decay. Lorentz, polarization, and Ψ-scan absorption corrections were applied using Crystal Logic software. Symmetry equivalent data were averaged

(33) Sheldrick, G. M. *SHELXS-86*: Structure Solving Program; University of Göttingen: Germany, 1986.
(34) Sheldrick, G. M. *SHELXL-97*: Crystal Structure Refinement Program; University of Göttingen: Germany, 1997.

with $R_{int} = 0.0127$ to give 6348 independent reflections from a total of 6520 collected. The structure was solved by direct methods using SHELXS-86[33] and refined by full-matrix least-squares techniques on F^2 with SHELXL-97[34] using 6348 reflections and refining 493 parameters. The compound crystallizes with two crystallographically independent CH_2Cl_2 and two H_2O solvate molecules per trinuclear complex. The solvate molecules showed large thermal motion parameters on their full occupancy; thus, the SQUEEZE option of PLATON program has been used to calculate and remove their contribution from the overall intensity data. All hydrogen atoms were introduced at calculated positions as riding on bonded atoms. All non-hydrogen atoms were refined anisotropically. The maximum and minimum residual peaks in the final difference map were 0.573 and −0.347 e Å^{-3}, respectively.

For **6**·4CH_2Cl_2, unit cell dimensions were determined and refined by using the angular settings of 25 automatically centered reflections in the range $22 < 2\theta < 54°$. Intensity data were recorded using a $\theta-2\theta$ scan to $2\theta_{max} = 113°$, with scan speed 1.5° min^{-1} and a scan range $2.45 + \alpha_1\alpha_2$ separation. The crystals showed poor diffraction ability (despite their sufficient size), and the data were collected in increasing 2θ shells. In the last data shell collection (104−113°) the observed data were less than 50% of the collected ones. Thus, the data collection was terminated. Three standard reflections monitored every 97 reflections showed less than 3% variation and no decay. Lorentz, polarization, and Ψ-scan absorption corrections were applied using Crystal Logic software. Symmetry equivalent data were averaged with $R_{int} = 0.0193$ to give 7647 independent reflections from a total of 7826 collected. The structure was solved by direct methods using SHELXS-86[33] and refined by full-matrix least-squares techniques on F^2 with SHELXL-97[34] using 7647 reflections and refining 639 parameters. The compound crystallizes with four crystallographically independent CH_2Cl_2 solvate molecules per trinuclear complex. The solvate molecules showed large thermal motion parameters on their full occupancy; thus, the SQUEEZE option of PLATON program has been used to calculate and remove their contribution from the overall intensity data. All hydrogen atoms were introduced at calculated positions as riding on bonded atoms. All non-hydrogen atoms were refined anisotropically. The maximum and minimum residual peaks in the final difference map were 0.388 and −0.666 e Å^{-3}, respectively.

Physical Measurements. Infrared spectra were recorded in the solid state (KBr pellets) on a Perkin-Elmer 16 PC FT spectrometer in the 4000−450 cm^{-1} range. Elemental analyses (C, H, and N) were performed on a Perkin-Elmer 2400 series II analyzer. Direct current (dc) and alternating current (ac) magnetic susceptibility studies were performed at the University of Florida Chemistry Department on a Quantum Design MPMS-XL SQUID susceptometer equipped with a 7 T magnet and operating in the 1.8−400 K range. Samples were embedded in solid eicosane to prevent torquing. Ac magnetic susceptibility measurements were performed in an oscillating ac field of 3.5 G and a zero dc field. The oscillation frequencies were in the 10−1488 Hz range. Magnetization versus field and temperature data were fit using the program MAGNET.[35] Pascal's constants were used to estimate the diamagnetic correction, which was subtracted from the experimental susceptibility to give the molar paramagnetic susceptibility (χ_M). Low-temperature (<1.8 K) hysteresis loop and dc relaxation measurements were performed at Grenoble using an array of micro-SQUIDS.[36] The high sensitivity of this magnetometer allows the study of single crystals of SMMs of the order of 10−500 μm. The field can be applied in any direction by separately driving three orthogonal coils.

High-frequency electron paramagnetic resonance (HFEPR) measurements were performed in the University of Florida Physics Department at various frequencies in the 60−170 GHz range. Single-crystal spectra were obtained at fixed microwave frequencies and temperatures using a sensitive cavity-perturbation technique. The fundamental mode of the cavity is 52 GHz, with higher-frequency measurements made possible by utilizing higher-order modes of the same cavity. A millimeter-wave vector network analyzer (MVNA) was employed as a source and detector; this instrumentation is described in detailed elsewhere.[37] Angle-dependent measurements were performed in a 7 T horizontal field magnet, allowing rotation of the sample about the vertical access port. This setup also allows rotation about an orthogonal axis using a rotating cavity,[37a,38] thereby enabling two-axis rotation measurements. Needle-shaped single crystals were removed directly from their mother liquor and protected with vacuum grease before cooling at 10 K min^{-1} under 1 atm of helium gas. Temperature control was achieved within the variable-flow cryostat belonging to a Quantum Design PPMS system.

Results and Discussion

Syntheses. The procedure employed was reaction of preformed $[Mn^{III}_3O(O_2CR)_6(py)_3]$-$(ClO_4)$ (R = Me (**1**), Et (**2**), Ph (**3**)) triangular complexes with 3 equivs of mpkoH in an MeCN/MeOH mixed-solvent medium. This reagent stoichiometry was chosen to potentially allow for the incorporation of one mpko$^-$ group onto each edge of the Mn_3 triangular core, although it could not, of course, have been predicted whether the reaction might instead yield a major change in the structure and/or nuclearity of the core. Nevertheless, evaporation of the obtained dark-brown solutions to dryness and crystallization of the residues from CH_2Cl_2/hexanes successfully gave dark-red crystals of $[Mn^{III}_3O(O_2CR)_3(mpko)_3](ClO_4)$ (R = Me (**4**), Et (**5**), Ph (**6**)) in high isolated yields (>80%), with almost colorless filtrates. The formation of complexes **4**−**6** is summarized in eq 1.

$$[Mn_3O(O_2CR)_6(py)_3]^+ + 3\ mpkoH \rightarrow [Mn_3O(O_2CR)_3(mpko)_3]^+ + 3\ RCO_2H + 3\ py \quad (1)$$

The reaction thus gave a simple ligand substitution, with no change to the metal oxidation level, leading to the replacement of three RCO_2^- and three py groups by three mpko$^-$ ones. The product was subsequently confirmed to have retained the Mn_3 core triangular structure, but with some small modifications (vide infra).[19,39] Since the Mn^{III}_3 complexes **1**−**3** had resulted in the Mn^{III}_3 products **4**−**6**, we also explored the same reactions between the neutral $[Mn_3O(O_2CR)_6(py)_2(H_2O)]$ ($Mn^{II}Mn^{III}_2$) triangular complexes, but these reactions also gave the same products **4**−**6** on addition of ClO_4^-, albeit in lower isolated yields of 45−55%.

Once the identity of the products **4**−**6** had been established, we also sought their synthesis from a more convenient procedure that does not employ any preformed triangular complexes but instead only simple starting materials. This was successfully accomplished from the comproportionation reaction between $Mn(O_2CR)_2$ and $NBu^n_4MnO_4$[40] in a 3:1 ratio in the presence of mpkoH and $NBu^n_4ClO_4$. Such comproportionation reactions between Mn^{II} and Mn^{VII} sources in the presence of appropriate

(35) Davidson, E. R. *MAGNET*; Indiana University: Bloomington, IN.
(36) Wernsdorfer, W. *Adv. Chem. Phys.* **2001**, *118*, 99.
(37) (a) Takahashi, S.; Hill, S. *Rev. Sci. Instrum.* **2005**, *76*, 023114. (b) Mola, M.; Hill, S.; Goy, P.; Gross, M. *Rev. Sci. Instrum.* **2000**, *71*, 186.
(38) Takahashi, S.; Edwards, R. S.; North, J. M.; Hill, S.; Dalal, N. S. *Phys. Rev. B* **2004**, *70*, 094429.
(39) Canada-Vilalta, C.; Streib, W. E.; Huffman, J. C.; O' Brien, T. A.; Davidson, E. R.; Christou, G. *Inorg. Chem.* **2004**, *43*, 101.
(40) Vincent, J. B.; Folting, K.; Huffman, J. C.; Christou, G. *Inorg. Chem.* **1986**, *25*, 996.

ligand groups have found extensive prior use to produce clusters of various nuclearities at the Mn^{III} and/or $Mn^{III/IV}$ oxidation level.[31,41] The ratio employed in this work gives, on paper, an average Mn oxidation state in solution of $Mn^{+3.25}$, slightly higher than the Mn^{3+} of **4**−**6**, but the MeOH solvent can act as a reducing agent if necessary. In any case, the yields of isolated products were in the 40−45% range, and it is possible there are other products in the colored filtrates, but we did not pursue their isolation. We did also explore the reaction with the Mn^{II}:Mn^{VII} ratio of 4:1 that gives an average Mn oxidation state of +3, but this led to products **4**−**6** contaminated with $[Mn_8O_2(OH)_2(O_2CR)_{10}(mpko)_4]$ ($4Mn^{II}$,$4Mn^{III}$). In addition, we investigated the use of smaller Mn^{II}:MnO_4^- ratios to give higher-average Mn oxidation states in the reaction (for example, a ratio of 3:2, which gives an average of Mn^{4+}), but these again gave only **4**−**6** in low (<20%) yields. These combined results suggest complexes **4**−**6** to be the thermodynamically favored products under these reaction conditions, a conclusion supported by the further observation that the use of >3 equivs of mpkoH in the reactions to see what type of cluster might result if more carboxylate groups were replaced led only to the same products **4**−**6** being isolated.

Description of Structures. Partially labeled plots of the cations of complexes **4**−**6** are shown in Figure 1. Selected interatomic distances and angles are listed in Table 2, and Mn−N−O−Mn torsion angles are listed in Table 3. Complexes **4** and **5** crystallize in the monoclinic space group $P2_1/c$, and complex **6**, in the monoclinic space group $P2_1/n$. The structures of the cations of **4**−**6** are very similar, and thus only the structure of representative complex **4** will be described in detail. The crystal structure of **4** consists of a $[Mn_3O(O_2CMe)_3(mpko)_3]^+$ cation, ClO_4^- anion, and lattice CH_2Cl_2 molecules. The cation consists of three Mn^{III} atoms in a triangular arrangement bridged by central μ_3-oxide atom O(61). Each edge of the Mn_3 triangle is bridged by an η^1:η^1:μ-$MeCO_2^-$ ion (**I**) and an η^1:η^1:η^1:μ-$mpko^-$ ligand (**II**), with the pyridyl and oximate nitrogen atoms chelating a Mn^{III} atom and forming a five-membered chelate ring. The Mn···Mn separations are almost equal (3.191(2)−3.203(2) Å); the triangle is thus scalene, and almost equilateral within the usual 3σ criterion. The oxidation states of all Mn atoms were established as +3 by charge balance considerations and inspection of Mn−O and Mn−N bond distances, and confirmed quantitatively by bond valence sum (BVS) calculations; these gave values of 2.72−2.83 for **4**.[42] BVS calculations also confirm that the central inorganic O atom is an O^{2-} ion, giving a value of 1.98 for O61 of **4**.

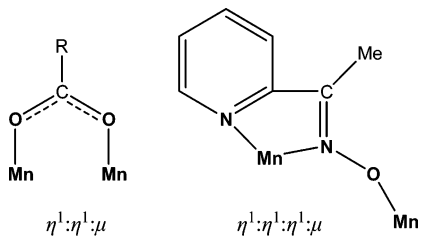

The three $MeCO_2^-$ groups lie on one side of the Mn_3 plane, and the three oximate groups on the other. The Mn atoms are near-octahedral, and the Mn^{III} centers exhibit a Jahn−Teller (JT) distortion, as expected for a high-spin d^4 ion in this geometry. As is almost always the case for Mn^{III} ions, the JT distortion is an axial elongation, typically of ∼0.1−0.2 Å for Mn−O bonds. The JT axes in **4** are the O(1)−Mn(1)−O(31), O(11)−Mn(2)−O(51), and O(21)−Mn(3)−O(42) axes, each involving carboxylate and oximate O atoms. Thus, as is almost always the case,

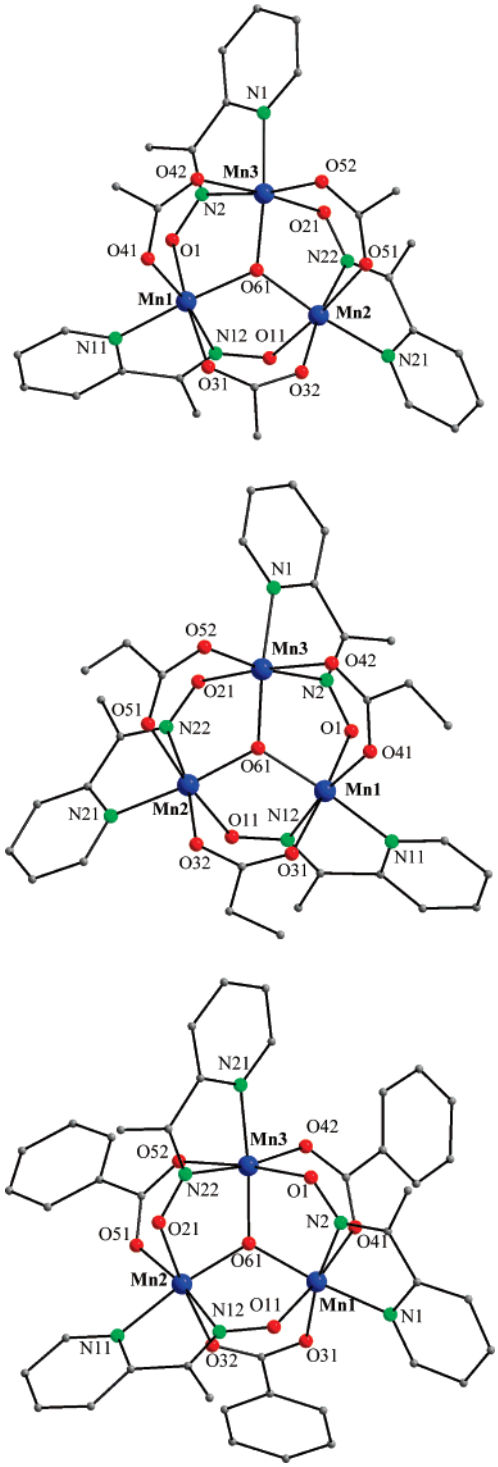

Figure 1. Structures of the cations present in complexes **4** (top), **5** (middle), and **6** (bottom).

(41) Harden, N. C.; Bolcar, M. A.; Wernsdorfer, W.; Abboud, K. A.; Streib, W. E.; Christou, G. *Inorg. Chem.* **2003**, *42*, 7067.

(42) (a) Brown, I. D.; Altermatt, D. *Acta Crystallogr.* **1985**, *B41*, 244. (b) Palenik, G. J. *Inorg. Chem.* **1997**, *36*, 4888. (c) Liu, W.; Thorp, H. H. *Inorg. Chem.* **1993**, *32*, 4102.

Table 2. Selected Interatomic Distances (Å) and Angles (deg) for Compounds **4**, **5**, and **6**

parameter	4	5	parameter	6
		Bond Distances		
Mn(1)···Mn(2)	3.191(2)	3.1974(15)	Mn(1)···Mn(2)	3.212(2)
Mn(1)···Mn(3)	3.193(2)	3.2060(17)	Mn(1)···Mn(3)	3.200(2)
Mn(2)···Mn(3)	3.203(2)	3.2101(13)	Mn(2)···Mn(3)	3.219(2)
Mn(1)−O(61)	1.870(4)	1.867(3)	Mn(1)−O(61)	1.880(3)
Mn(1)−O(41)	1.918(4)	1.932(4)	Mn(1)−O(31)	1.940(3)
Mn(1)−O(31)	2.178(4)	2.198(4)	Mn(1)−O(41)	2.190(4)
Mn(1)−O(1)	2.173(5)	2.182(4)	Mn(1)−O(11)	2.180(4)
Mn(1)−N(12)	2.008(5)	2.015(4)	Mn(1)−N(2)	2.006(4)
Mn(1)−N(11)	2.020(5)	2.040(4)	Mn(1)−N(1)	2.021(4)
Mn(2)−O(61)	1.867(4)	1.873(3)	Mn(2)−O(61)	1.882(3)
Mn(2)−O(32)	1.925(4)	1.922(4)	Mn(2)−O(51)	1.926(3)
Mn(2)−O(51)	2.216(4)	2.219(4)	Mn(2)−O(32)	2.217(3)
Mn(2)−O(11)	2.205(4)	2.207(4)	Mn(2)−O(21)	2.165(3)
Mn(2)−N(22)	2.011(5)	2.017(4)	Mn(2)−N(12)	2.020(4)
Mn(2)−N(21)	2.052(5)	2.043(5)	Mn(2)−N(21)	2.049(4)
Mn(3)−O(61)	1.867(4)	1.879(3)	Mn(3)−O(61)	1.864(3)
Mn(3)−O(52)	1.926(4)	1.930(4)	Mn(3)−O(42)	1.944(4)
Mn(3)−O(42)	2.205(4)	2.211(4)	Mn(3)−O(52)	2.234(3)
Mn(3)−O(21)	2.193(4)	2.191(4)	Mn(3)−O(1)	2.180(3)
Mn(3)−N(2)	2.012(4)	2.014(4)	Mn(3)−N(22)	2.010(4)
Mn(3)−N(1)	2.042(4)	2.046(4)	Mn(3)−N(21)	2.028(4)
		Bond Angles		
Mn(1)−O(61)−Mn(2)	117.25(19)	117.48(17)	Mn(1)−O(61)−Mn(2)	117.24(16)
Mn(1)−O(61)−Mn(3)	117.37(18)	117.71(17)	Mn(1)−O(61)−Mn(3)	117.43(15)
Mn(2)−O(61)−Mn(3)	118.09(18)	117.64(17)	Mn(2)−O(61)−Mn(3)	118.49(16)
N(11)−Mn(1)−O(61)	169.29(19)	169.12(17)	N(1)−Mn(1)−O(61)	169.90(16)
N(21)−Mn(2)−O(61)	168.99(19)	169.97(19)	N(11)−Mn(2)−O(61)	169.10(14)
N(1)−Mn(3)−O(61)	168.93(18)	169.06(16)	N(21)−Mn(3)−O(61)	168.64(16)

Table 3. Mn−N−O−Mn Torsion Angles (ψ, deg) for Complexes **4**−**6**

	4	5	6
Mn(1)−N(12)−O(11)−Mn(2)	10.1	9.6	15.4
Mn(2)−N(22)−O(21)−Mn(3)	10.9	12.2	9.6
Mn(3)−N(2)−O(1)−Mn(1)	12.5	10.1	14.2
average	11.2	10.6	13.1

the JT elongation axes avoid the $Mn^{III}-O^{2-}$ bonds,[43] the shortest and strongest in the cation.

The central oxide atom O61 of **4** is 0.294 Å above the Mn_3 plane on the same side as the carboxylate groups, and the three $Mn-O^{2-}$ bonds are equal (1.867(4)−1.870(4) Å) and comparable with those reported for other complexes containing the $[Mn^{III}_3(\mu_3\text{-O})]^{7+}$ core.[44] The $Mn-O^{2-}-Mn$ angles are also all equal, in the range 117.3(2)−118.1(2)°.[45] The structures of the cations of **5** and **6** are essentially identical to that of **4**. In particular, the O^{2-} ions in **5** and **6** are 0.293 and 0.286 Å, respectively, above the Mn_3 planes. Complexes **4**−**6** join a small family of structurally characterized metal complexes that contain mpko$^-$ ligands,[46−49] but they are the first examples with Mn. Note that mpko$^-$ has been observed in these other complexes to also display a variety of other ligation modes spanning η^2,[46] η^1,[47], $\eta^1:\eta^1:\eta^1:\mu$,[47b,48] $\eta^1:\eta^1:\mu$,[47a,b] and $\eta^1:\eta^1:\eta^2:\mu_3$[49] modes.

Comparison of the Structures of 4−6 with other $[Mn^{III}_3(\mu_3\text{-O})]^{7+}$ Complexes. It will be of great relevance to the magnetic properties of **4**−**6** discussed below to compare their structures with those of the $[Mn_3O(O_2CR)_6(py)_3]^+$ starting materials and other related complexes with a $[Mn^{III}_3(\mu_3\text{-O})]^{7+}$ core. The latter is not uncommon in Mn(III) chemistry.[44] Several $[Mn_3O(O_2CR)_6L_3]^+$ (L = monodentate ligand) complexes have been reported,[44b−d] and their crystallographic data reveal that (i) the μ_3-O^{2-} ion lies in the Mn_3 plane and (ii) there is an essentially planar Mn−O−C−O−Mn unit, i.e., each carboxylate group is coplanar with the two Mn^{III} ions that it bridges (deviations from this planarity are small, as measured by the Mn−O−O−Mn torsion angle of typically 1−5°). Essentially the same situation applies even in the complex $[Mn_3O(mpdp)_3(py)_3](ClO_4)$,[39,44e] where a dicarboxylate ligand *m*-phenylenedipropionate (mpdp^{2-}) replaces the two carboxylate groups bridging each Mn^{III}_2 edge. Three carboxylate-free $[Mn^{III}_3(\mu_3$-

(43) Chakov, N. E.; Lee, S.-C.; Harter, A. G.; Kuhns, P. L.; Reyes, A. P.; Hill, S. O.; Dalal, N. S.; Wernsdorfer, W.; Abboud, K. A.; Christou, G. *J. Am. Chem. Soc.* **2006**, *128*, 6975.

(44) (a) Bhula, R.; Gainsford, G. J.; Weatherburn, D. C. *J. Am. Chem. Soc.* **1988**, *110*, 7550. (b) Wu, R.; Poyraz, M.; Sowrey, F. E.; Anson, C. E.; Wocadlo, S.; Powell, A. K.; Jayasooriya, U. A.; Cannon, R. D.; Nakamoto, T.; Katada, M.; Sano, H. *Inorg. Chem.* **1998**, *37*, 1913. (c) An, J.; Chen, Z.-D.; Bian, J.; Jin, X.-L.; Wang, S.-X.; Xu, G.-X. *Inorg. Chim. Acta* **1999**, *287*, 82. (d) Li, J.; Yang, S.; Zhang, F.; Tang, Z.; Ma, S.; Shi, Q.; Wu, Q.; Huang, Z. *Inorg. Chim. Acta* **1999**, *294*, 109. (e) Canada-Vilalta, C.; Huffman, J. C.; Streib, W. E.; Davidson, E. R.; Christou, G. *Polyhedron* **2001**, *20*, 1375. (f) Sreerama, S. G.; Pal, S. *Inorg. Chem.* **2002**, *41*, 4843. (g) Nihei, M.; Hoshino, N.; Ito, T.; Oshio, H. *Chem. Lett.* **2002**, 1016. (h) Jones, L. F.; Raftery, J.; Teat, S. J.; Collison, D.; Brechin, E. K. *Polyhedron* **2005**, *24*, 2443.

(45) (a) Milios, C. J.; Kyritsis, P.; Raptopoulou, C. P.; Terzis, A.; Vicente, R.; Escuer, A.; Perlepes, S. P. *Dalton Trans.* **2005**, 501. (b) Brechin, E. K.; Sanudo, E. C.; Wernsdorfer, W.; Boskovic, C.; Yoo, J.; Hendrickson, D. N.; Yamaguchi, A.; Ishimoto, H.; Concolino, T. E.; Rheingold, A. L.; Christou, G. *Inorg. Chem.* **2005**, *44*, 502.

(46) (a) Stamatatos, Th. C.; Bell, A.; Cooper, P.; Terzis, A.; Raptopoulou, C. P.; Heath, S. L.; Winpenny, R. E. P.; Perlepes, S. P. *Inorg. Chem. Commun.* **2005**, *8*, 533. (b) Riggle, K.; Lynde-Kernell, T.; Schlemper, E. O. *J. Coord. Chem.* **1992**, *25*, 117. (c) Rajunen, A.; Orama, M.; Saarinen, H. *Acta Crystallogr.* **1999**, *55C*, 2075. (d) Lynde-Kernell, T.; Schlemper, E. O. *J. Coord. Chem.* **1988**, *16*, 347. (e) Phelps, D. W.; Little, W. F.; Hodgson, D. J. *Inorg. Chem.* **1976**, *15*, 2263.

(47) (a) Sharma, V.; Sharma, R. K.; Bohra, R.; Ratnani, R.; Jain, V. K.; Drake, J. E.; Hursthouse, M. B.; Light, M. E. *J. Organomet. Chem.* **2002**, *651*, 98. (b) Sharma, V.; Sharma, R. K.; Jain, V. K.; Drake, J. E.; Light, M. E.; Hursthouse, M. B. *J. Organomet. Chem.* **2002**, *664*, 66. (c) Gupta, A.; Sharma, R. K.; Bohra, R.; Jain, V. K.; Drake, J. E.; Hursthouse, M. B.; Light, M. E. *Polyhedron* **2002**, *21*, 2387.

(48) Papatriantafyllopoulou, C.; Raptopoulou, C. P.; Terzis, A.; Manessi-Zoupa, E.; Perlepes, S. P. *Z. Naturforsch.* **2006**, *61b*, 1.

(49) Papatriantafyllopoulou, C.; Aromi, G.; Tasiopoulos, A. J.; Nastopoulos, V.; Raptopoulou, C. P.; Teat, S. J.; Escuer, A.; Perlepes, S. P. *Eur. J. Inorg. Chem.* **2007**, 2761.

O)]$^{7+}$ complexes have also been structurally characterized: $[Mn_3O(bamen)_3](ClO_4)$,[44f] (bamen^{2-} = 1,2-bis(biacetylmonoximeimino)ethanate), $[Mn_3O(5\text{-Br-sap})_3(H_2O)_3]Cl$,[44g] (5-Br-sap^{2-} = 2-(5-bromosalicylideneamino)-1-propanolate), and $(NHEt_3)_2[Mn_3O(bta)_6F_3]$,[14,44h] (bta$^-$ = benzotriazolate). The only previous $[Mn^{III}_3(\mu_3\text{-O})]^{7+}$ complex that, like **4**−**6**, contains *both* carboxylate and non-carboxylate ligands is the unusual $[Mn_3O(O_2CMe)_2(O_2)(dien)_3)]I_3$,[44a] where a μ-peroxide group bridges one of the Mn_2 edges. In all these complexes except $[Mn_3O(5\text{-Br-sap})_3(H_2O)_3]Cl$,[44g] the O^{2-} group lies exactly in the Mn_3 plane, or essentially so (<0.02 Å), although the available structural data for $[Mn_3O(O_2CMe)_2(O_2)(dien)_3)]^{3+}$ [44a] do not permit an exact determination of the planarity of the $[Mn_3(\mu_3\text{-}O^{2-})]$ unit. The exception $[Mn_3O(5\text{-Br-sap})_3(H_2O)_3]Cl$[44g] is due to the edges being mono-atomically bridged giving a partial-cubane $[Mn^{III}_3(\mu_3\text{-O})(\mu\text{-OR})_3]^{4+}$ core, with the central O^{2-} ion ~0.8 Å above the Mn_3 plane.

Given the above, the distinct displacement of the μ_3-O^{2-} ion in **4**−**6** from the Mn_3 plane was surprising, and we rationalize it as follows: the replacement of a triatomic carboxylate bridge with a diatomic oximate one would by itself likely favor a slight shortening of the Mn···Mn separations, which can only occur with retention of the preferred Mn−O^{2-} bond distances if the O^{2-} ion moves out of the Mn_3 plane. The latter is facilitated by the expected nonplanarity of the Mn−N−O−Mn unit of the mpko$^-$ group, which is twisted slightly as reflected in the torsion angles (ψ) about the N−O bond of 9.6−15.4° (Table 3). But each mpko$^-$ group does not just replace a carboxylate one; its pyridyl group also replaces the terminal pyridine group in the starting material. However, the mpko$^-$ pyridyl group cannot perfectly reach around to bind in a preferred manner on the Mn atom without introducing excessive strain, and we believe this is relieved by the μ_3-O^{2-} ion being additionally displaced from the Mn_3 plane. This effectively causes a tilting of the Mn coordination axes permitting binding of the pyridyl group onto the Mn atom. In spite of this, there is still some strain, as reflected in the nonlinearity of the O^{2-}−Mn−N axes (Figure 1), which are ~168−170° rather than ~180°. The net result is a shortening of the Mn···Mn separations in **4**−**6** (~3.2 Å), compared with those in the $[Mn_3O(O_2CR)_6L_3]^+$ complexes (3.27−3.45 Å), and a total displacement of the μ_3-O^{2-} ion by ~0.3 Å from the Mn_3 plane. An important consequence of this is that the angle (θ) between the Jahn−Teller axis of each Mn^{III} atom and the Mn_3 plane is increased in **4**−**6** compared with those in the $[Mn_3O(O_2CR)_6L_3]^+$ complexes, with average values of 60.7°, 59.6°, and 59.1° for **4**−**6**, respectively. In contrast, the $[Mn_3O(O_2CR)_6L_3]^+$ complexes typically have θ values of ~46−48° with the Mn_3 plane. The combined structural details described above are crucial in determining both the ground-state spin S value and the ZFS parameter D of **4**−**6**, as will be discussed below.

Magnetochemistry

Direct Current Magnetic Susceptibility Studies. Variable-temperature magnetic susceptibility measurements were performed on powdered polycrystalline samples of complexes **4**, **5**·H_2O, and **6**·2.5H_2O, restrained in eicosane to prevent torquing, in a 1 kG (0.1 T) field and in the 5.0−300 K range. The data are shown as $\chi_M T$ vs T plots in Figure 2.

The $\chi_M T$ for **4** increases from 13.01 cm^3 mol^{-1} K at 300 K to a maximum of 19.39 cm^3 mol^{-1} K at 30 K and then decreases

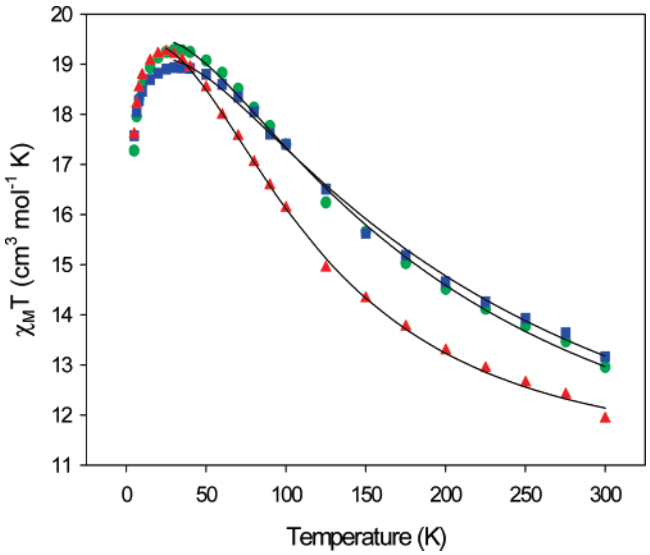

Figure 2. $\chi_M T$ vs T for polycrystalline samples of complexes **4** (green ●), **5** (red ▲), and **6** (blue ■) in a 1 kG field. The solid lines are the fits of the data to the theoretical expression; see Table 4 for the fit parameters.

to 17.41 cm^3 mol^{-1} K at 5.0 K. Complex **5**·H_2O exhibits similar behavior, with $\chi_M T$ increasing from 11.92 cm^3 mol^{-1} K at 300 K to a maximum of 19.25 cm^3 mol^{-1} K at 25.0 K, and then decreasing to 17.60 cm^3 mol^{-1} K at 5.0 K. Finally, complex **6**·2.5H_2O shows an increase in $\chi_M T$ from 13.16 cm^3 mol^{-1} K at 300 K to a maximum of 18.93 cm^3 mol^{-1} K at 30.0 K, followed by a decrease to 19.08 cm^3 mol^{-1} K at 5.0 K. The maxima for the three complexes are slightly below the spin-only ($g = 2$) value expected for a complex with an $S = 6$ ground state (21.00 cm^3 mol^{-1} K), and this is consistent with $g < 2.0$ as expected for Mn. The decrease in the $\chi_M T$ value at the lowest temperatures is likely due to zero-field splitting (ZFS), Zeeman effects from the applied field, and any weak intermolecular antiferromagnetic exchange interactions. At higher temperatures, the decrease in $\chi_M T$ is due to the thermal population of excited states with $S < 6$.

To determine the individual pairwise exchange parameters J_{ij} between Mn_iMn_j pairs within the molecule, the $\chi_M T$ vs T data for complexes **4**−**6** were fit to the appropriate theoretical expression for a Mn^{III}_3 triangle. We used an isosceles triangle model since the complexes are approximately equilateral but nevertheless do not possess crystallographic C_3 symmetry in the solid state; in any case, even crystallographically equilateral $[M_3O]$ triangles are known to undergo the magnetic Jahn−Teller distortion,[50] resulting in an isosceles situation. The isosceles model requires two exchange parameters (J), and the resulting isotropic Heisenberg spin Hamiltonian is given by eq 2,

$$H = -2J(\hat{S}_1\cdot\hat{S}_2 + \hat{S}_1\cdot\hat{S}_{2'}) - 2J'\hat{S}_2\cdot\hat{S}_{2'} \qquad (2)$$

where $J = J_{12} = J_{12'}$ and $J' = J_{22'}$ refer to the $Mn^{III}Mn^{III}$ exchange interactions of a C_{2v} symmetry isosceles triangle with Mn2−Mn2′ being the unique edge.

Applying the Kambe approach[51] using the substitutions $\hat{S}_A = \hat{S}_2 + \hat{S}_{2'}$ and $\hat{S}_T = \hat{S}_A + \hat{S}_1$, where S_T is the total spin of the

(50) Cannon, R. D.; Jayasooriya, U. A.; Wu, R.; arapKoske, S. K.; Stride, J. A.; Nielsen, O. F.; White, R. P.; Kearley, G. J.; Summerfields, D. *J. Am. Chem. Soc.* **1994**, *116*, 11869 and references therein.
(51) Kambe, K. *J. Phys. Soc. Jpn.* **1950**, *5*, 48.

Table 4. Magnetism Fit Parameters and Selected Structural Parameters for **4**−**6**

complex	$J^{a,b}$	$J'^{a,c}$	g	d^{d}	ψ^{e}	$\Delta(N_{ox})^{f}$	$\Delta(O_{ox})^{f}$	θ^{g}
4 (R = Me)	14.1	3.8	1.91	0.294	11.2	0.067	0.062	60.7
5 (R = Et)	12.1	1.5	1.92	0.293	10.7	0.066	0.062	59.6
6 (R = Ph)	18.6	6.7	1.92	0.286	13.1	0.077	0.072	59.1

[a] cm^{-1}. [b] ±1.2 cm^{-1}. [c] ± 0.5 cm^{-1}. [d] d is the distance (Å) of the μ_3-O^{2-} ion from the Mn_3 plane. [e] ψ is the average Mn−N−O−Mn torsion angle (deg) from Table 3. [f] Δ is the average displacement (Å) of the indicated atom from the oxime Mn−N−O−Mn least-squares plane. [g] θ is the average angle (deg) between the JT elongation axes and the Mn_3 plane.

whole molecule, gives the equivalent spin Hamiltonian of eq 3.

$$H = -J(\hat{S}_T^{\,2} - \hat{S}_A^{\,2} - \hat{S}_1^{\,2}) - J'(\hat{S}_A^{\,2} - \hat{S}_2^{\,2} - \hat{S}_{2'}^{\,2}) \quad (3)$$

The eigenvalues of eq 3 are given by eq 4, where $E(S_T, S_A)$ is the energy of state S_T arising from S_A, and constant terms contributing to all states have been omitted.

$$E(S_T, S_A) = -J[S_T(S_T + 1) - S_A(S_A + 1)] - J'[S_A(S_A + 1)] \quad (4)$$

For complexes **4**−**6**, $S_1 = S_2 = S_{2'} = 2$, and the overall multiplicity of the spin system is 125, made up of 19 individual spin states ranging from $S_T = 0$ to 6.

A theoretical $\chi_M T$ vs T expression was derived using the S_T values, their energies $E(S_T)$, and the Van Vleck equation, and this expression was used to fit the experimental data. Data below 30 K were omitted because the low-temperature decrease is caused by factors not included in the above model. The fit parameters were J, J', and g. A temperature-independent paramagnetism (TIP) term was included, held fixed at 600×10^{-6} cm^3 mol^{-1}. Good fits were obtained for all three complexes, and these are shown as solid lines in Figure 2. Fits of the data for **4**−**6** to a one-J model (i.e., $J = J'$) for a C_3 equilateral triangle gave poor fits and g significantly greater than 2.0.

The fit parameters are collected in Table 4, and the main conclusion is thus that the exchange interactions in **4**−**6** are ferromagnetic giving an $S_T = 6$ ground state, the $|S_T,S_A\rangle = |6,4\rangle$ state. Both J and J' are relatively weak, and there is a noticeable difference between them. It should be noted, however, that the difference of approximately 10 cm^{-1} is small in an absolute sense, and the complexes can reasonably be described as magnetically almost an equilateral situation but with a small range of J values as a result of the solid-state symmetry being lower than C_3. Note also that the observed J and J' values are the net small differences between larger and competing antiferromagnetic (negative J) and ferromagnetic (positive J) interactions among the three d^4 Mn^{III} ions, according to eq 5.

$$J_{obs} = J_{AF} + J_F \quad (5)$$

Thus, as is typical of small differences between large numbers, only relatively small changes to the competing J_{AF} and J_F contributions will appear as more significant differences to their sum, i.e., J and J'.

Further examination of Table 4 shows that the exchange interactions are quite similar in the three complexes, as expected given their overall very similar structures. Nevertheless, J and J' for **6** do appear to be slightly stronger than those for **4** and **5**. Examination of the selected structural parameters in Table 4 shows a small, but we believe real, correlation with the differences in J and J'. Thus, **6** has the strongest J and J', the smallest displacement of its μ_3-O^{2-} ion from the Mn_3 plane (d), and the largest oxime torsion angle (ψ). The latter, of course, is also reflected in the greatest deviations of the oxime N and O atoms from the Mn−N−O−Mn least-squares plane (Δ). We shall attempt to rationalize these observations later (vide infra).

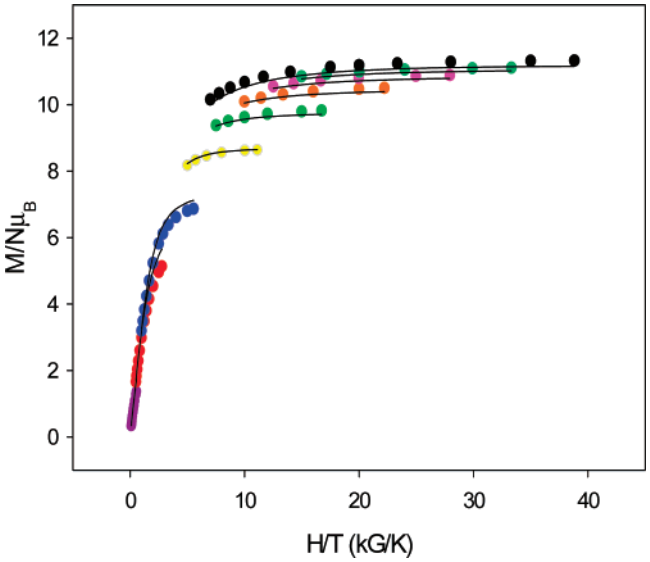

Figure 3. Plot of reduced magnetization ($M/N\mu_B$) vs H/T for complex **4** at 0.1 (magenta ●), 0.5 (red ●), 1.0 (blue ●), 2.0 (yellow ●), 3.0 (green ●), 4.0 (orange ●), 5.0 (pink ●), 6.0 (dark green ●), and 7.0 (black ●) T. The solid lines are the fit of the data; see the text for the fit parameters.

Magnetization versus Dc Magnetic Field Studies. To confirm the $S_T = 6$ ground-state spin and to determine the magnitude of the zero-field splitting parameter D, magnetization vs dc field measurements were made for restrained samples of complexes **4**, **5**·H_2O, and **6**·$2.5H_2O$ at applied magnetic fields and temperatures in the 10−70 kG and 1.8−10.0 K ranges, respectively. The data for representative complex **4** are shown in Figure 3 as reduced magnetization ($M/N\mu_B$) *vs* H/T plots, where M is the magnetization, N is Avogadro's number, μ_B is the Bohr magneton, and H is the magnetic field. For complexes populating only the ground state and possessing no axial zero-field splitting (ZFS), i.e. $D = 0$, the magnetization versus field plot follows the Brillouin function, and the isofield lines superimpose and saturate at a value of gS. However, the experimental data of complex **4** in Figure 3 clearly do not superimpose, indicating significant magnetic anisotropy (ZFS) in the ground state.

The $M/N\mu_B$ versus H/T data were fit using the program MAGNET[35] to a model that assumes only that the ground state is populated at these temperatures and magnetic fields, includes isotropic Zeeman interactions and axial zero-field splitting ($D\hat{S}_z^2$), and incorporates a full powder average.[10a,52] The corresponding spin Hamiltonian is given by eq 6,

(52) Yoo, J.; Yamaguchi, A.; Nakano, M.; Krzystek, J.; Streib, W. E.; Brunel, L.- C.; Ishimoto, H.; Christou, G.; Hendrickson, D. N. *Inorg. Chem.* **2001**, *40*, 4604.

$$\hat{H} = D\hat{S}_z^2 + g\mu_B\mu_0\hat{S}\cdot H \quad (6)$$

where D is the axial ZFS parameter, $\hat{S}_z$ is the easy-axis spin operator, μ_0 is the vacuum permeability, and H is the applied field. The last term in eq 6 is the Zeeman energy associated with an applied magnetic field. The best fit for **4** is shown in Figure 3; the fits for the other compounds (see Supporting Information) were of comparable quality. The fit parameters were $S = 6$ for all complexes, with the following D and g values: -0.34 cm^{-1} and 1.92 for **4**, -0.34 cm^{-1} and 1.93 for **5**·H_2O, and -0.35 cm^{-1} and 1.99 for **6**. We confirmed that these were the global fit minima by running root-mean-square D versus g error surfaces for the fits using the program GRID,[35] which calculates the relative difference between the experimental $M/N\mu_B$ data and those calculated for various combinations of D and g. The error surface (Figure S2 of Supporting Information) indeed displays a single, fairly hard minimum, indicating a relatively small level of uncertainty in the best-fit parameters. However, the high-frequency EPR (HFEPR) data to be described (vide infra) indicated that complex **4** possesses a not-insignificant rhombic zero-field splitting parameter E, and we realized that we should thus be including both D and E in the magnetization fits of **4**−**6**. Shown in Figure 4 is the error surface for the D vs E fit of the magnetization data with a fixed $g = 2.0$, as indicated by the accurate HFEPR technique. The D and E fit parameters were -0.26 and 0.013 cm^{-1} for **4**, -0.25 and 0.012 cm^{-1} for **5**·H_2O, and -0.34 and 0.015 cm^{-1} for **6**·2.5H_2O. Fixing the g at 1.99 gave the same D and E values for **4** to two significant figures.

The $S = 6$ value of complexes **4**−**6**, together with a significant anisotropy as reflected in the appreciable D value, suggested they might possess a significant barrier (U) to magnetization relaxation and thus possibly be SMMs; U is the barrier for relaxation between the $M_s = \pm 6$ levels. As mentioned in the Introduction, the upper limit to this barrier is given by $U = S^2|D|$ for an integer spin system, or $36|D|$ for $S = 6$, although the actual or effective barrier (U_{eff}) is significantly less due to quantum tunneling of the magnetization (QTM) through the barrier via higher energy M_s levels. We thus decided to investigate the magnetization dynamics of these complexes using ac magnetic susceptibility studies.

Alternating Current Magnetic Susceptibility Studies. Ac studies were performed in the 1.8−10 K range using a 3.5 G ac field oscillating at frequencies in the 10−498 Hz range. If the magnetization vector can relax fast enough to keep up with the oscillating field, then there is no imaginary (out-of-phase) susceptibility signal (χ''_M), and the real (in-phase) susceptibility (χ'_M) is equal to the dc susceptibility.[53] However, if the barrier to magnetization relaxation is significant compared to thermal energy (kT), then there is a nonzero χ''_M signal and the in-phase signal decreases. In addition, the χ''_M signal will be frequency-dependent. Such frequency-dependent χ''_M signals are a characteristic signature of the superparamagnetic-like properties of a SMM (but by themselves do not prove the presence of a SMM[54]). For complexes **4**, **5**·H_2O, and **6**·2.5H_2O, the in-phase χ'_M signal above approximately 6 K is almost temperature independent and extrapolates to a value in the of 18−19 cm^3 mol^{-1} K range at 0 K, consistent with an $S = 6$ ground state and $g < 2$.[55] The plots for representative complex **6**·2.5H_2O are shown in Figure 5; those for the other complexes are in Supporting Information. At lower temperatures, the effects of anisotropy, weak intermolecular interactions, and slow relaxation (below 3.0 K) lead to a decrease in the χ'_M signal. Below 3 K, tails of frequency-dependent χ''_M signals appear, suggestive of the superparamagnet-like slow relaxation of a SMM. The χ''_M peak maxima clearly lie at temperatures below 1.8 K, the operating minimum temperature of our SQUID magnetometer.

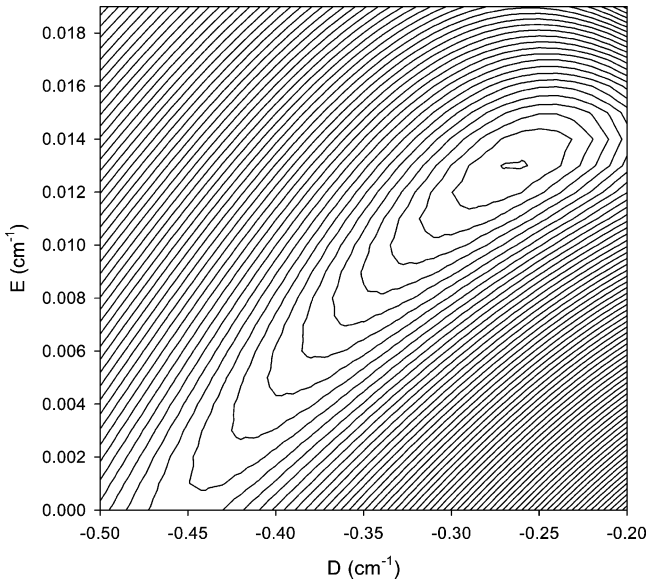

Figure 4. Two-dimensional contour plot of the root-mean-square error surface for the D vs E fit for complex **4**.

The in-phase $\chi'_M T$ vs T plot for **6**·2.5H_2O in Figure 5 is almost temperature-independent down to 3 K or so where the sharp decreases due to slow relaxation become manifested, whereas those for **4** and **5**·H_2O show more of a decrease between 10 and 3 K. We assign this to the bulkier carboxylate groups of $[Mn_3O(O_2CPh)_3(mpko)_3](ClO_4)$ (**6**) resulting in weaker intermolecular interactions compared with **4** and **5**. As a result, a clear χ''_M peak maximum is seen for **6**·2.5H_2O at 498 Hz, whereas **4** and **5**·H_2O have all peak maxima below 1.8 K.

Magnetization versus Dc Field Hysteresis Loops. With the combined dc and ac susceptibility studies revealing that complexes **4**−**6** have an $S = 6$ ground state, a significant D value of ~ -0.3 cm^{-1}, and exhibit out-of-phase ac signals suggestive of a SMM, we carried out magnetization (M) versus dc field studies to look for hysteresis behavior, the diagnostic property of a magnet. Magnetization versus applied dc field data were collected on single-crystals of **4**·3CH_2Cl_2 (that had been kept in contact with mother liquor) using a micro-SQUID apparatus.[36] Because there are two different orientations of Mn_3 molecules in the crystal, the external field was applied at an

(53) Novak, M. A.; Sessoli, R. In *Quantum Tunnelling of Magnetization*, QTM'94; Gunther, L., Barbar, B., Eds.; Kluwer: Dordrecht, The Netherlands, 1995; pp 171−188.

(54) (a) Chakov, N. E.; Wernsdorfer, W.; Abboud, K. A.; Christou, G. *Inorg. Chem.* **2004**, *43*, 5919. (b) Mishra, A.; Tasiopoulos, A. J.; Wernsdorfer, W.; Abboud, K. A.; Christou, G. *Inorg. Chem.* **2007**, *46*, 3105.

(55) (a) Soler, M.; Wernsdorfer, W.; Folting, K.; Pink, M.; Christou, G. *J. Am. Chem. Soc.* **2004**, *126*, 2156. (b) Sanudo, E. C.; Wernsdorfer, W.; Abboud, K. A.; Christou, G. *Inorg. Chem.* **2004**, *43*, 4137. (c) Murugesu, M.; Habrych, M.; Wernsdorfer, W.; Abboud, K. A.; Christou, G. *J. Am. Chem. Soc.* **2004**, *126*, 4766.

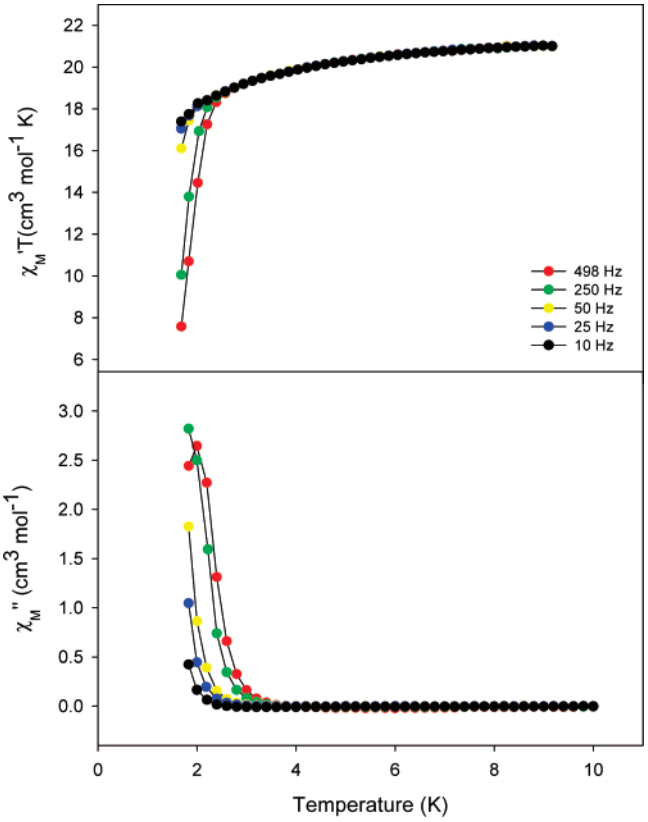

Figure 5. Plot of the in-phase (χ'_M) (as $\chi'_M T$) and out-of-phase (χ''_M) AC susceptibility signals of complex **6**·2.5H_2O in a 3.5 G field oscillating at the indicated frequencies.

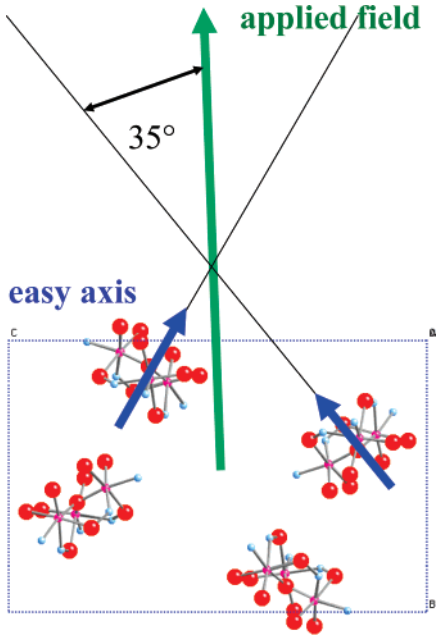

Figure 6. Diagram showing the two easy-axis orientations in a crystal of **4**·3CH_2Cl_2 (blue) and the applied dc field direction (green).

angle of ∼35°, intermediate to the two easy-axis (*z*-axis) orientations, as shown in Figure 6. The resulting magnetization vs dc field responses are shown in Figure 7, which includes both a temperature dependence at a constant field sweep rate of 0.14 T/s (Figure 7, top) and a field sweep rate dependence at a constant temperature of 0.04 K (Figure 7, bottom). Hysteresis loops were indeed observed below ∼1.0 K, whose

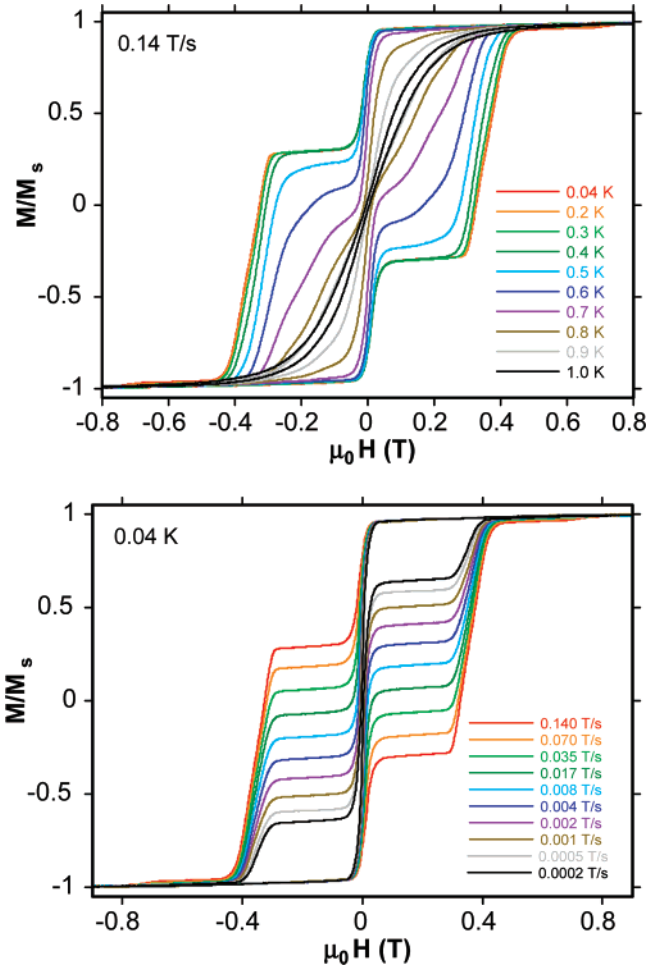

Figure 7. Magnetization (*M*) vs dc field (*H*) hysteresis loops for a single-crystal of **4**·3CH_2Cl_2 at (top) a constant scan rate of 0.14 T/s and the indicated temperatures, and (bottom) at the indicated field sweep rates and a fixed temperature of 0.04 K. The magnetization is normalized to its saturation value, M_s.

coercivities increase with decreasing temperature and increasing field sweep rate, as expected for the superparamagnetic-like properties of a SMM below its blocking temperature (T_B). The data thus indicate complex **4**·3CH_2Cl_2 to be a new addition to the family of SMM, the first with a triangular [$M_3(\mu_3$-O)] metal topology. The blocking temperature (T_B) is ∼1.0 K, above which there is no hysteresis; that is, the spin relaxes faster to equilibrium than the time scale of the hysteresis loop measurement.

The clearly dominating feature of the hysteresis loops in Figure 7 is the large QTM step at zero field, which indicates that quantum tunneling in zero field is so fast (corresponding to ∼35% reversal of the magnetization at 0.04 K and 0.14 T/s, and ∼80% reversal at 0.0002 T/s) that there often appears to be no coercivity at $M/M_s = 0$. However, at other positions, the coercivity is clearly temperature- and time (sweep rate)-dependent, increasing with decreasing temperature and increasing sweep rate, indicative of the superparamagnetic-like properties of a SMM.

Steps at periodic values of applied field are a diagnostic signature of resonant QTM[6a,56] and have been seen for several distinct classes of SMMs, such as the Mn_{12} family in three oxidation states (i.e., the $[Mn_{12}O_{12}(O_2CR)_{16}(H_2O)_4]^z$ (z = 0, 1,

2) complexes[17,18,57]), Fe_8,[58] and the Mn_4 complexes with C_{3v} virtual symmetry.[59] In all cases, the first step in sweeping the field from one saturating value to the other occurs at zero field where the potential energy double-well is symmetric and M_s levels on one side of the barrier are degenerate (in resonance) with those on the other side, allowing tunneling to occur through the anisotropy barrier. The steps are thus positions of increased magnetization relaxation rate. The separation between steps, ΔH, is proportional to D, as given in eq 7,

$$\Delta H = k|D|/g\mu_B \cos(\alpha) \tag{7}$$

where k is the Boltzmann constant, and α is the bisecting angle (deg) between the applied dc field and the resulting easy axes of the molecule; in the case of **4**·$3CH_2Cl_2$, the angle α is 35°. Measurement of the step positions in Figure 7 gave an average ΔH of 0.355 T and thus a $|D|/g$ value of 0.14 cm^{-1} (0.20 K). Assuming $g = 2.0$, this corresponds to a D value of 0.28 cm^{-1} = 0.39 K, in excellent agreement with the values from the reduced magnetization fit for *dried* samples of **4** (D = 0.26 cm^{-1} for $g = 2.0$; $|D|/g$ = 0.13 cm^{-1} = 0.19 K). Note that at such low temperatures there is not enough thermal energy to overcome the potential energy barrier, and essentially all magnetization relaxation is by QTM involving a two-phonon Orbach process via higher-lying M_s levels where the tunneling rates are faster. However, Figure 7 (top) shows that the hysteresis loops become essentially temperature-independent below ~0.3 K, indicating only ground-state QTM from the lowest-lying $M_s = -6$ level to the $M_s = +6$ is occurring below this temperature.

Relaxation Studies Using Ac and Dc Data. Two methods were combined in order to obtain data that would allow a more quantitative investigation of the magnetization relaxation dynamics of **4**·$3CH_2Cl_2$. Further ac χ''_M studies were carried out on a single crystal down to 1.1 K, and the data are plotted as χ''_M versus frequency (f) in Figure 8 (top). At a given temperature, the position of the χ''_M peak maximum is the point at which the angular frequency ($\omega = 2\pi f$) of the oscillating field equals the magnetization relaxation rate ($1/\tau$, where τ is the relaxation time); relaxation rate versus T data can thus be obtained from the position of the peak maxima and this $\omega = 1/\tau$ relationship. For relaxation rate versus T data to lower temperatures, the crystal's magnetization was first saturated in one direction at ~5 K with a large applied dc field, the temperature decreased to a chosen value in the 0.04−0.85 K range, and then the field removed and the magnetization decay monitored with time (Figure S6, top).

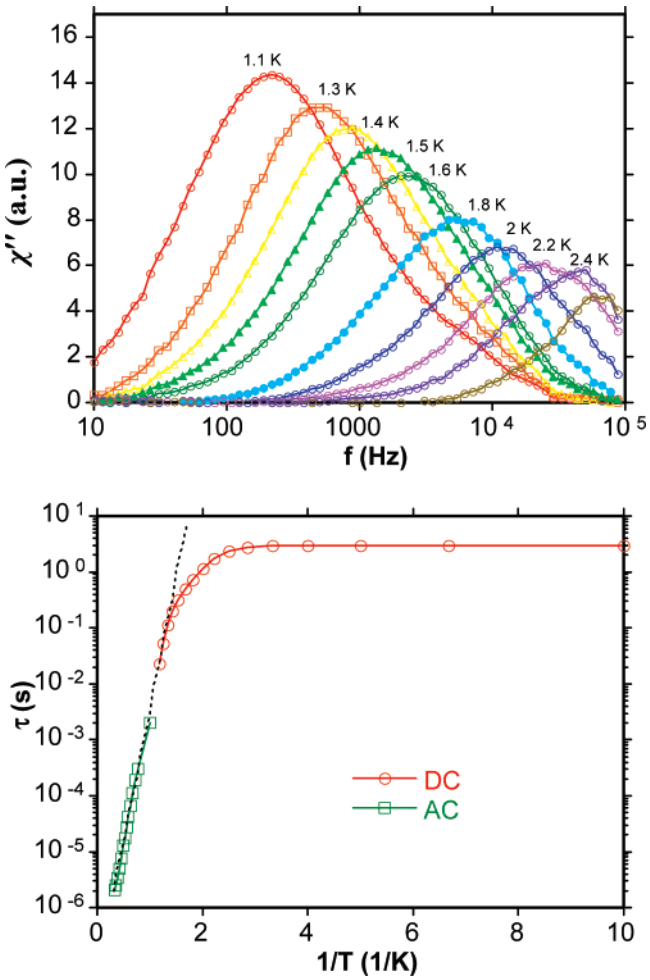

Figure 8. Plots for **4**·$3CH_2Cl_2$ of (top) the out-of-phase (χ'') ac susceptibility versus frequency at the indicated temperatures, and (bottom) the relaxation time (τ) vs $1/T$ using AC χ''_M and DC magnetization decay data. The dashed line is the fit of the thermally activated region to the Arrhenius equation. See the text for the fit parameters.

The obtained relaxation rate ($1/\tau$) versus T data from the combined ac and dc studies were used to construct an Arrhenius plot, shown as τ versus $1/T$ in Figure 8 (bottom). The magnetization relaxation of a SMM obeys the Arrhenius relationship of eq 8,

$$(1/\tau) = (1/\tau_0)\exp(-U_{eff}/kT) \tag{8a}$$

$$\ln(1/\tau) = \ln(1/\tau_0) - U_{eff}/kT \tag{8b}$$

the characteristic behavior of a thermally activated Orbach process, where U_{eff} is the effective energy barrier and k is the Boltzmann constant. The fit to the thermally activated region above ~0.3 K gave $\tau_0 = 5.7 \times 10^{-8}$ s and U_{eff} = 10.9 K. The mean barrier U_{eff} is smaller than the calculated $U = S^2|D|$ = 12.2 K, as expected for QTM between higher energy M_s levels of the $S = 6$ manifold. In other words, the system does not have to get to the top of the barrier (i.e., the $M_s = 0$ level), but instead can tunnel through the barrier from some lower M_s level. At 0.3 K and below, the relaxation becomes temperature independent, consistent with relaxation by ground-state QTM. In other words, tunneling is now only between the lowest-energy $M_s = \pm 6$ levels, and no longer via a thermally (phonon) assisted pathway involving higher-energy M_s levels. The crossover

(56) (a) Friedman, J. R.; Sarachik, M. P.; Tejada, J.; Maciejewski, J.; Ziolo, R. *J. Appl. Phys.* **1996**, *79*, 6031. (b) Sangregorio, C.; Ohm, T.; Paulsen, C.; Sessoli, R.; Gatteschi, D. *Phys. Rev. Lett.* **1997**, *78*, 4645. (c) Brechin, E. K.; Soler, M.; Christou, G.; Helliwell, M.; Teat, S. J.; Wernsdorfer, W. *Chem. Commun.* **2003**, 1276.

(57) (a) Sessoli, R.; Tsai, H.-L.; Schake, A. R.; Wang, S.; Vincent, J. B.; Folting, K.; Gatteschi, D.; Christou, G.; Hendrickson, D. N. *J. Am. Chem. Soc.* **1993**, *115*, 1804. (b) Tsai, H.-L.; Hendrickson, D. N.; Eppley, J. J.; de Vries, N.; Folting, K.; Christou, G. *J. Chem. Soc., Chem. Commun.* **1994**, 1745. (c) Aubin, S. M. J.; Sun, Z.; Guzei, I. A.; Rheingold, A. L.; Christou, G.; Hendrickson, D. N. *J. Chem. Soc., Chem. Commun.* **1997**, 2239. (d) Kuroda-Sowa, T.; Nakano, M.; Christou, G.; Hendrickson, D. N. *Polyhedron* **2001**, *20*, 1537.

(58) Caneschi, A.; Ohm, T.; Paulsen, C.; Rovai, D.; Sangregorio, C.; Sessoli, R. *J. Magn. Magn. Mater.* **1998**, *177*, 1330.

(59) (a) Wang, S.; Wemple, M. S.; Tsai, H.-L.; Folting, K.; Huffman, J. C.; Hagen, K. S.; Hendrickson, D. N.; Christou, G. *Inorg. Chem.* **2000**, *39*, 1501. (b) Wang, S.; Tsai, H.-L.; Hagen, K. S.; Hendrickson, D. N.; Christou, G. *J. Am. Chem. Soc.* **1994**, *116*, 8376. (c) Aromi, G.; Bhaduri, S.; Artús, P.; Folting, K.; Christou, G. *Inorg. Chem.* **2002**, *41*, 805.

temperature between thermally activated relaxation and ground-state tunneling is between 0.2 and 0.3 K.

Single-Crystal, High-Frequency EPR (HFEPR) Spectroscopy. The analysis of EPR spectra for high-spin complexes can provide precise information such as the exact value of the ground-state spin,[60] the magnitude and sign of D,[61] the location in energy of excited spin states relative to the ground state,[62] and most importantly, information concerning transverse spin Hamiltonian parameters that are responsible for the QTM, e.g., the rhombic E-term.[63] However, the $(2S+1)$-fold energy level structure associated with a large molecular spin S necessitates EPR spectroscopy spanning a wide frequency range.[64] Furthermore, large ZFS due to the significant crystalline anisotropy and large S_T values demand the use of frequencies and magnetic fields considerably higher (40 GHz to several 100 GHz, up to 10 T) than those typically used by the majority of EPR spectroscopists.[64,65]

The complete Hamiltonian (H) that describes the Mn_3 compounds is given in eq 9.

$$H = D\hat{S}_z^2 + \mu_o g \mu_B \hat{S}\cdot H + E(\hat{S}_x^2 - \hat{S}_y^2) + B_4\hat{O}_4 \qquad (9)$$

This is the same as eq 6, but with additional terms. The third term parametrizes the rhombic distortion, i.e., the dominant transverse ZFS term that likely causes the QTM and is the main focus of these EPR studies; E ($<|D/3|$) is the rhombic ZFS parameter, and $\hat{S}_x$ and $\hat{S}_y$ are the x- and y-axis spin component operators. The final term represents fourth-order ZFS interactions, e.g., $B_4^0\hat{O}_4^0$.[66] The other symbols have the meanings defined earlier.

The HFEPR study of complex **4**·$3CH_2Cl_2$ is complicated by the two orientations of the magnetic axes, neither of which aligns with the principal crystallographic axes (Figure 6). Shown in Figure 9 are angle-dependent spectra taken at 62 GHz and 5 K. The appearance of multiple peaks spanning a wide field range is indicative of a molecular species with an appreciable spin S and significant anisotropy.[67] Assuming easy-axis anisotropy ($D < 0$), one expects to see the strongest peaks appearing at low fields when the field is aligned near to the easy axis, while the strongest peaks should appear at high fields when the field is in the hard plane. The data in Figure 9 exhibit both of these behaviors. Since the orientation of the crystal was not known *a priori*, we did not know the exact plane of rotation. However, for 180° rotation we are guaranteed to pass through the hard planes associated with both sites (not necessarily coincidentally); we are also likely to pass close to the easy axes, but it is not guaranteed that we will hit those directions exactly. As can be seen, there exist two field orientations (54° and 108°, colored blue) exhibiting essentially identical spectra, with strong EPR peaks extending to the highest fields. These orientations correspond to the hard planes associated with each lattice site.

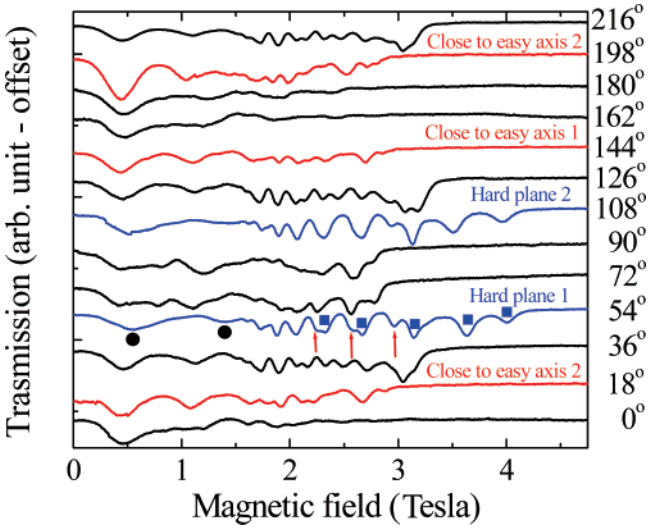

Figure 9. Angle-dependent spectra taken at 62 GHz and 5 K on a single crystal of **4**·$3CH_2Cl_2$ at the indicated angles. The blue curves correspond to the directions of the two hard planes. The red curves correspond to the closest approaches to the two easy axes. For the 54° trace, the blue squares mark the resonances corresponding to the field parallel to hard plane 1 (species 1); the low-field peaks marked with black dots are remnants of the easy-axis spectra for species 2, while the higher-field peaks marked with red arrows are remnants of the hard-plane spectra (see text). The field is oriented ~42° from the easy axis of species 2.

The obtained separation of the hard planes (~54°) is significantly less than the ~70° separation of the easy axes associated with the two species, which implies that the plane of rotation is inclined to the plane containing the two easy-axis directions. Consequently, for any given field orientation, one can observe many components of the spectrum. For example, in the 54° trace, there are two independent sets of more-or-less evenly spaced peaks at high fields marked by blue squares and red arrows. The higher-field set (blue squares) corresponds to the main peaks associated with one of the hard planes (species 1); the field is exactly in the hard plane for these sites. Meanwhile, the field is ~50° from the other hard plane and ~40° from the easy axis associated with the other sites (species 2). Therefore, one can also observe remnants of both the easy-axis (broad low-field peaks marked by black dots) and the hard-plane spectrum (sharper peaks at intermediate fields marked by red arrows) for species 2 in the 54° data. The field approaches closest to the easy-axis directions when 90° away from the hard planes, i.e., 18°, 144° and 198°. One can see from these traces (colored red) that the spectra do resemble easy-axis data at low fields, i.e., broader, well-spaced peaks decreasing in strength with increasing field.[68]

Figure 10 displays the angle dependence of the strongest peak positions obtained at 129 GHz. For a uniaxial system (easy axis or easy plane) in the high-field limit, $g\mu_B B \gg DS$ (= 2 T for Mn_3), one expects each peak to approximately follow a $(1 - 3\cos^2\theta)$ angle dependence about the isotropic position ($g = 2$ line), where θ is the orientation of the field relative to the principal (z) axis (not the experimental angle from Figure 10).

(60) Edwards, R. S.; Maccagnano, S.; Yang, E.- C.; Hill, S.; Wernsdorfer, W.; Hendrickson, D. N.; Christou, G. *J. Appl. Phys.* **2003**, *93*, 7807.
(61) Rumberger, E.; Hill, S.; Edwards, R. S.; Wernsdorfer, W.; Zakharov, L. N.; Rheingold, A. L.; Christou, G.; Hendrickson, D. N. *Polyhedron* **2003**, *22*, 1865.
(62) Petukhov, K.; Hill, S.; Chakov, N. E.; Christou, G. *Phys. Rev. B* **2004,** *70*, 054426.
(63) Hill, S.; Edwards, R. S.; Jones, S. I.; North, J. M.; Dalal, N. S. *Phys. Rev. Lett.* **2003**, *90*, 217204.
(64) Hill, S.; Edwards, R. S.; Jones, S. I.; Maccagnano, S.; North, J. M.; Aliaga, N.; Yang, E.- C.; Dalal, N. S.; Christou, G.; Hendrickson, D. N. *Mater. Res. Soc. Symp. Proc.* **2003**, *746*, 253. (Materials Research Society).
(65) (a) Hill, S.; Dalal, N. S.; Brooks, J. S. *Appl. Magn. Reson.* **1999**, *16*, 237. (b) Mola, M.; Hill, S.; Goy, P.; Gross, M. *Rev. Sci. Instrum.* **2000**, *71*, 186.
(66) (a) Park, K.; Novotny, M. A.; Dalal, N. S.; Hill, S.; Rikvold, P. A. *Phys. Rev. B* **2002**, *65*, 14426. (b) Park, K.; Novotny, M. A.; Dalal, N. S.; Hill, S.; Rikvold, P. A. *Phys. Rev. B* **2002**, *66*, 144409.
(67) Hill, S.; Perenboom, A. J.; Dalal, N. S.; Hathaway, T.; Stalcup, T.; Brooks, J. S. *Phys. Rev. Lett.* **1998**, *80*, 2453.
(68) Hill, S.; Maccagnano, S.; Park, K.; Achey, R. M.; North, J. M.; Dalal, N. S. *Phys. Rev. B* **2002**, *65*, 224410.

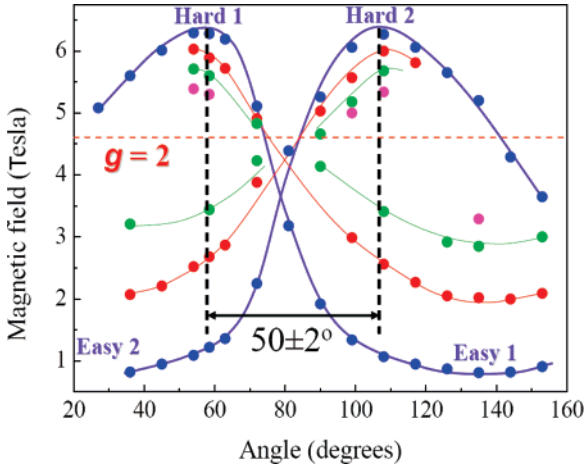

Figure 10. EPR peak positions versus angle from data obtained at 5 K at a higher frequency of 129 GHz. Each peak exhibits an asymmetric two-fold pattern (180° periodicity). The hard and easy directions are indicated for each species; the solid lines are guides. The $g = 2$ line for a frequency of 129 GHz is also shown as a guide.

As can be seen, each peak does oscillate about $g = 2$, and the deviation to the low-field side (field close to z) of $g = 2$ is roughly twice the deviation to the high-field side (field parallel to xy) for each transition. Assuming $D < 0$ (see below), the locations of the two hard planes (dashed vertical lines) were estimated from the maxima of the blue curves. However, the curves deviate significantly from the ideal $(1 - 3\cos^2\theta)$ dependence. There are several reasons for this. First, the $g\mu_B B \gg DS$ condition is not satisfied over the entire field range; this causes sharper maxima and broader minima. Second, the field rotation plane is not orthogonal to the two hard planes. Consequently, there is a variation in the in-plane field component for each species as the magnetic field is rotated. If there were no in-plane anisotropy, the angle dependence would be symmetric about the hard-plane directions. This is clearly not the case. Consequently, there must be two anisotropies at play, one which depends only on the out-of-plane field component which is symmetric about the hard plane, and another that depends only on the in-plane field component, which need not necessarily be symmetric about the hard plane.

In order to quantify the ZFS parameters, frequency-dependent measurements were performed with the magnetic field applied within the hard plane of species 1, corresponding to 54° in Figure 9 (hard plane 1). The positions of the observed resonances are plotted in the frequency versus field plot of Figure 11b. The peak positions were then simulated using the spin Hamiltonian of eq 9. The red curves were matched to the red low-field data points and the blue curves to the high-field blue data points. We made the assumption that the field was exactly in the hard plane for the blue curves, while the orientation of the field was adjusted for the red curves. In doing so, we were able to obtain agreement with all peak positions, using just a single set of ZFS parameters, as expected since the two lattice sites are related by a simple rotation. Thus, the only difference between the red and blue curves in Figure 11b is the orientation of the magnetic field relative to the z-axis of the molecules. We did start out by assuming $S = 6$. However, simulations with larger and smaller S values gave significantly poorer agreement, i.e. Figure 11b provides independent confirmation of the $S = 6$ ground state deduced from the bulk magnetization measurements.[63]

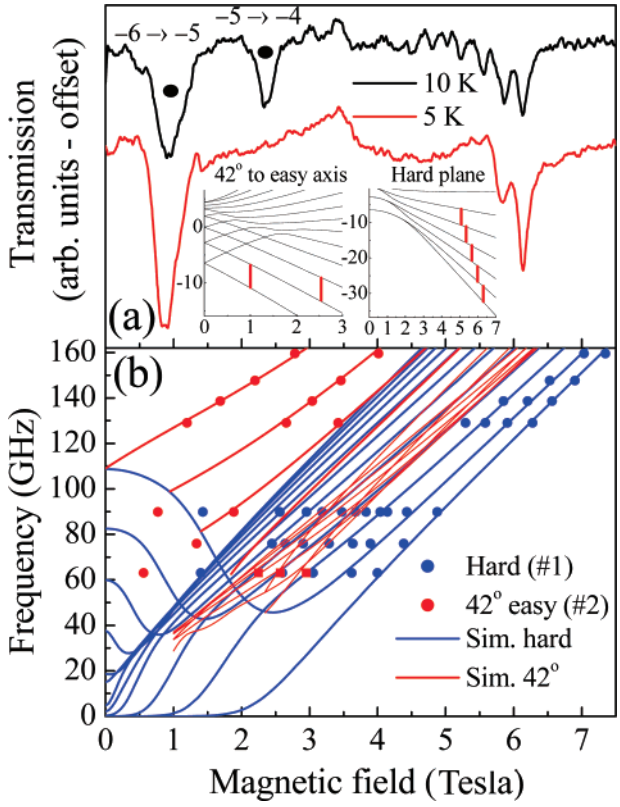

Figure 11. (a) Temperature dependence of the 129 GHz spectra with the field parallel to hard plane 1 (54°). The two insets display the Zeeman diagrams generated using the obtained ZFS parameters for two field orientations: 42° away from the easy axis (left) and parallel to the hard plane (right). The red bars in these insets represent the observed EPR transitions. The low-field transitions have been labeled according to the M_s values involved in the transitions. (b) Frequency dependence of the main EPR peaks at 5 K for the field applied parallel to hard plane 1 (54°). The solid blue and red circles correspond to species 1 and 2, respectively; the solid red squares correspond to the peaks marked by red arrows in Figure 9. The solid lines are simulations yielding the ZFS parameters given in the main text. The blue curves correspond to fields applied in the hard plane for species 1, and red curves for fields applied 42° from the easy axis of species 2.

The red data in Figure 11b place the strongest constraint on the axial D and B_4^0 parameters, as well as determining the orientation of the field relative to the easy axis of the species 2. In order to maintain a good fit to the low-field data, while simultaneously fitting the blue data points, we found it necessary to include a significant transverse anisotropy. Since we do not know the exact plane of rotation, we cannot determine the precise value of the transverse anisotropy parameter. Furthermore, we cannot determine its symmetry, as has been done for other SMMs via field rotation studies.[63,69] Nevertheless, to get some idea of the degree of transverse anisotropy, we use the standard rhombic interaction of the form $E(\hat{S}_x^2 - \hat{S}_y^2)$.[70] The best agreement between experiment and simulation gave $D = -0.3\ \text{cm}^{-1}$, $B_4^0 = -3 \times 10^{-5}\ \text{cm}^{-1}$, $g = 2.00$, and a significant $E \geq 0.015\ \text{cm}^{-1}$. For species 2, the field is found to be $42 \pm 2°$ away from the easy axis ($48 \pm 2°$ away from the hard plane), which agrees with the angle-dependent measurements. The

(69) del Barco, E.; Kent, A. D.; Hill, S.; North, J. M.; Dalal, N. S.; Rumberger, E. M.; Hendrickson, D. N.; Chakov, N.; Christou, G. *J. Low Temp. Phys.* **2005**, *140*, 119.
(70) Barra, A. L.; Gatteschi, D.; Sessoli, R. *Chem. Eur. J.* **2000**, *6*, 1608.

reason for the lower bound on E is because our fits assumed that the field was precisely along the hard axis for the high-field data points (species 1, blue data points). One could include a larger E value and rotate the field slightly toward the medium axis (within the hard plane) and obtain an equally good fit. To put this in context, the E/D ratio of 0.05 is about a quarter of that found for the biaxial Fe_8 SMM.[58] The thin red lines correspond to simulations of the peaks marked by red arrows in Figure 9; three data points (red squares) are also included. The slight deviation between the red square positions and the thin red curves may be attributed to the fact that we do not know the precise orientation of the field within the hard plane.

Finally, Figure 11a displays 129 GHz data obtained at 10 and 5 K with the field parallel to the hard plane of species 1. The two insets display the Zeeman diagrams generated using the obtained ZFS parameters for two field orientations: 42° away from the easy axis (left) and parallel to the hard plane (right). The red bars in these insets represent the observed EPR transitions. As can be seen, the EPR intensity transfers to the lowest and highest field peaks upon lowering the temperature, i.e., the transitions from the lowest-lying levels in the two Zeeman diagrams. This behavior can only be explained by assuming a negative D value. Consequently, the temperature dependence provides spectroscopic confirmation of a negative sign of D, thereby verifying that complex **4** is in fact a SMM, the first with a triangular topology.

Rationalization of the Switching on of the SMM Property. The primary reason that complexes **4**−**6** are new SMMs is that they possess a large $S = 6$ ground state, and thus the main question that remains to be addressed is why are they ferromagnetically coupled, whereas the starting $[Mn^{III}_3O(O_2CR)_6(py)_3]^+$ complexes **1**−**3** are antiferromagnetically coupled? The obvious first thing to be stated is that it must be a consequence of the structural distortions imposed on the molecule by the replacement of three carboxylate bridges by three oximate ones. Note that bridging oximate ligands usually give antiferromagnetic interactions, as do carboxylates, so this replacement *per se* cannot be the origin of the switch in the interaction. Clearly, the latter must instead be the result of the two structural changes to the core, the displacement (d) of the central μ_3-O^{2-} ion out of the Mn_3 plane, and the twist in the Mn−N−O−Mn bridging unit as reflected in the torsion angle ψ. The displacement d is expected to be important because it has long been recognized that strongly bonded, monoatomically bridging O^{2-} ions represent excellent mediators of exchange interactions and thus provide the primary exchange pathways in metal oxide clusters. However, with metals such as Mn^{III}, which possess both empty and partially occupied d orbitals, the net observed J value (J_{obs}) between two interacting metal ions is the sum of competing ferromagnetic (J_F) and antiferromagnetic (J_{AF}) interactions, as summarized in eq 5.[71]

An important, predicted consequence of the displacement of the μ_3-O^{2-} ion out of the Mn_3 plane is that $|J_{AF}|$ should decrease as M−O−M d_π−p_π−d_π orbital overlaps are weakened by rehybridization of the bridging O atom as it converts from trigonal planar to trigonal pyramidal. Note that overlap of π-symmetry magnetic orbitals is the primary contribution to the antiferromagnetic exchange between Mn^{III} atoms, since the local Mn^{III} z-axis is defined by the JT elongation axis and the σ-symmetry $d_{x^2-y^2}$ orbital (oriented toward the μ_3-O^{2-} ion) is thus empty.

Since the net J_{obs} within $[Mn^{III}_3O(O_2CR)_6(py)_3]^+$ complexes is only weakly antiferromagnetic, with $|J| = |J_{obs}| < 11$ cm^{-1} [21] a weakening of the antiferromagnetic contribution (J_{AF}) in eq 5 will lead to an even weaker antiferromagnetic net J_{obs} and thus even to the observed ferromagnetic one. It is not anticipated that the J_F will be significantly affected by the displacement d. However, the data in Table 4 indicate that the displacement d cannot be the only factor influencing the net exchange coupling, because the magnitude of the two parameters J and J' do not correlate perfectly with d. In fact, d for benzoate complex **6** is slightly smaller than those for **4** and **5**, and yet it has the strongest ferromagnetic J and J' values. If the latter correlated directly with d, they should be smaller (weaker) for **6**. Instead, it appears that J and J' are also dependent on the oxime twist defined by the torsion angle ψ, with the largest ψ being that for complex **6**, which has the largest J and J' values (Table 4). Such a twist in the oxime will lead to a corresponding twist/tilting of the Mn coordinate axes, which will again cause a subtle weakening of M−O−M d_π−p_π−d_π orbital overlaps and thus give a net increase in the positive J_{obs} from eq 5. It will require DFT calculations to probe this effect in a more quantitative manner, and to assess the relative importance of the displacement d and torsion angle ψ, but note that the twisting of oxime bridges has also subsequently provided the basis for the switching of all the exchange parameters in hexanuclear Mn^{III}_6 complexes to ferromagnetic, providing a new family of $S = 12$ SMMs with the highest anisotropy barriers yet observed.[16]

Also important to the observed behavior of Mn_3 complexes **4**−**6** as SMMs is the anisotropy of the molecules, as gauged by the axial ZFS parameter D. This is because the anisotropy barrier to magnetization reorientation scales as $S^2|D|$, as mentioned earlier. Remembering that the molecular anisotropy is the tensor projection of the single-ion anisotropies onto the molecular anisotropy axis, it can easily be seen that the structural distortions imposed by the bridging mpko$^-$ groups will also influence the molecular D value. The single-ion Mn^{III} anisotropy axes (z axes) are the JT elongation axes, and the molecular anisotropy axis (i.e. the easy axis) is perpendicular to the Mn_3 plane. This is as expected from the structure of the molecule, because the JT axes are at an angle θ with the Mn_3 plane. Given the virtual C_3 rotation symmetry of the molecules, there will be little net anisotropy projected into the Mn_3 (xy) plane, but significant anisotropy perpendicular to it along the molecular z-axis. Further, the fact that the angle θ increases by 10−15° in **4**−**6** vs **1**−**3** helps to enhance the molecular anisotropy of the former, i.e., even with the spin being raised to $S = 6$, the barrier to magnetization relaxation in **4**−**6** would have been expected to be significantly smaller if the JT axes had not also been tilted further from the Mn_3 plane. A relevant example that demonstrates such an increase in the anisotropy parameter D when the Mn^{III} JT axes of a Mn^{III}_3 plane are tilted so that they are "more parallel" to the z-axis (i.e. θ is larger) is provided by our previous study by HFEPR and magnetization fits of the $[Mn_4O_3(O_2CR)_4(dbm)_3]$ family of SMMs with $S = {}^9/_2$, where dbm$^-$ is the anion of dibenzoylmethane.[10a,f] Similar conclusions

(71) Hotzelmann, R.; Wieghardt, K.; Florke, U.; Haupt, H.-J.; Weatherburn, D. C.; Bonvoisin, J.; Blondin, G.; Girerd, J.-J. *J. Am. Chem. Soc.* **1992**, *114*, 1681.

were reached from a study by inelastic neutron scattering of the $[Mn_4O_3X(O_2CMe)_3(dbm)_3]$ family of SMMs, where X = F^-, Cl^-, or Br^-.[72] The overall conclusion is therefore that the structural distortions in **4**−**6** vs those in **1**−**3** serve to make the former new examples of SMMs because both (i) the coupling is switched to ferromagnetic, giving a large spin $S = 6$ ground state and (ii) the JT axes are tilted further from the Mn_3 plane, ensuring a significant molecular axial anisotropy, D.

Conclusions

We have shown that the structural distortion imposed on $[Mn_3O(O_2CR)_6(L)_3]^+$ complexes by binding of tridentate oximate ligands switches the exchange coupling to ferromagnetic and makes **4**−**6** the initial examples of triangular SMMs. It has been tempting in the past to conclude that members of the venerable class of triangular $[M_3O(O_2CR)_6(L)_3]^{0,+}$ complexes possessing the oxide-centered $[M_3(\mu_3\text{-O})]$ cores could never provide new examples of SMMs because (a) the exchange interactions are antiferromagnetic and thus the molecules possess small or zero ground state S values and (b) the C_3 symmetric structure with local anisotropy axes relatively close to the Mn_3 plane leads to small molecular anisotropy. However, the present work has shown that relatively small, ligand-imposed structural distortions can alter the sign of the exchange interactions in $[Mn_3(\mu_3\text{-O})]^{7+}$ complexes and "switch on" the SMM property. We emphasize again that this oximate-induced effect is caused by two contributions, both important to the SMM property: (i) an increase in the spin to $S = 6$, the maximum possible for three Mn^{III} ions, by the coupling becoming ferromagnetic, and (ii) the presence of a significant molecular easy-axis anisotropy (i.e., $|D|$ value) caused by a large angle between the JT elongation axes and the Mn_3 hard plane (xy plane).

The overall outcome of the above is that single-molecule magnetism within an additional structural type has now been established. In fact, we suggested when this work was communicated[29] that application of this strategy of altering the sign of the exchange interactions within triangular (or other) structures with chelating and/or bridging ligands might lead to additional new examples of SMMs. Indeed, this has since been realized with the recent results with hexanuclear Mn^{III}_6 complexes that structurally are dimers of Mn_3 triangles, and which can be converted from $S = 4$ to $S = 12$ by ligand-induced structural distortions imposed by oxime ligands. This was strictly speaking not a switching on of the SMM property, since the $S = 4$ species was also an SMM, but the $S = 12$ has a much bigger barrier, the biggest for any SMM to date.

Finally, we return to our statement in the Introduction that there are two general strategies for making new SMMs: the first is to seek completely new structural types that might have the necessary high S and D values to function as SMMs, which requires the use of new types of ligands and/or development of new synthetic methods, and the second is to modify known structural types that may or may not already be SMMs in their own right. The present results represent a new approach within the second strategy, namely the conversion of a non-SMM into an SMM without changing the identity of core bridging atoms or the electron count, but instead by introducing a ligand-induced structural perturbation of the magnetic core. This work has thus provided a proof-of-feasibility for this approach.

Acknowledgment. S.P.P. thanks the European Social Fund (ESF), Operational Program for Educational and Vocational Training II (EPEAEK II), and the Program PYTHAGORAS (Grant b.365.037). S.O.H. (DMR-0239481) and G.C. (CHE-0414555) thank the U.S.A. National Science Foundation for funding.

Supporting Information Available: X-ray crystallographic files in CIF format, tables with selected bond distances (Å) and angles (deg), and various magnetism figures as mentioned in the text for complexes **4**−**6**. This material is available free of charge via the Internet at http://pubs.acs.org.

JA072194P

(72) (a) Andres, H.; Basler, R.; Gudel, H.-U.; Aromi, G.; Christou, G.; Buttner, H.; Ruffle, B. *J. Am. Chem. Soc.* **2000**, *122*, 12469. (b) Sieber, A.; Chaboussant, G.; Bircher, R.; Boskovic, C.; Güdel, H. U.; Christou, G.; Mutka, H. *Phys. Rev. B*, **2004**, *70*, 172413 (1−4).